P. D'Antuono, M. Morandini
Thermal Shock Response via Weakly Coupled Peridynamic Thermo-Mechanics
International Journal of Solids and Structures, Vol. 129, 2017, p. 74-89
doi:10.1016/j.ijsolstr.2017.09.010

Thermal shock response via weakly coupled peridynamic thermo-mechanics

Pietro D'Antuono[a], Marco Morandini[b,*]

[a] *Politecnico di Bari, Dipartimento di Meccanica, Matematica e Management, viale Japigia 182, 70126 Bari, Italy*
[b] *Politecnico di Milano, Dipartimento di Scienze e Tecnologie Aerospaziali, via La Masa 34, 20156 Milano, Italy*

Abstract

A 3D peridynamic formulation of the thermo-mechanical problem allows to efficiently simulate the occurrence and propagation of cracks due to extreme thermal loading. The model is weakly coupled since no internal heat generation due to material deformation and damage is accounted for. As such, it is suitable to simulate low strain rate phenomena. Since the typical time scales of the mechanical and thermal systems may differ of several orders of magnitude, using a multirate explicit integration technique is suggested by the nature of the problem itself. Finally, the proposed formulation is used to model the thermal shock behavior of thin and thick slabs, in order to observe respectively a 2D ordered set of parallel cracks and a 3D honeycomb crack pattern addressed as columnar jointing.

Keywords: Peridynamics; brittle failure; thermal shock; ceramics; thermo-mechanics.

1. Introduction

Most of the theories developed to simulate fracture nucleation and propagation are based on the local continuum theory. The effectiveness of standard finite elements for such problems is however severely impaired by the well-known mesh-dependency of the solution and the need to remesh the domain

*Corresponding author.
Email addresses: pietro.dantuono@poliba.it (Pietro D'Antuono), marco.morandini@polimi.it (Marco Morandini)

as the fracture propagates. Many numerical techniques have been developed so far in order to overcome some of the above mentioned shortcomings of the standard FEM; among them, the cohesive elements, meshless methods and the eXtended-FEM (X-FEM) are worth citing. Cohesive elements bypass the mesh-dependency problem by explicitly accounting for the finite dimension of the elements, thus allowing to account for a proper energy balance, as shown by e.g. Wells and Sluys (2001) and de Borst et al. (2004). Meshless methods allow to easily adapt the discretization in order to follow the crack tip, see e.g. Belytschko et al. (1996). This is often balanced by an increased overall complexity of the numerical formulation, as well summarized by Nguyen et al. (2008). The X-FEM allows to account for fracture propagation without the need to remesh the domain, see e.g. Moës and Belytschko (2002); similar, simplified techniques can be applied also to meshfree methods, as shown e.g. by Rabczuk and Belytschko (2004). The regularized variational formulation proposed by Bourdin et al. (2013) is also worth citing.

A completely different class of approaches for the study of fracture formation and propagation is based on the direct application of Newtonian mechanics. These techniques are based on networks of concentrated masses connected by springs, and have been used, among other things, to study columnar fracture process in granule-water mixtures (Nishimoto et al., 2007), crack propagation in crystals (Hayakawa, 1994a,b), failure of brittle materials (Curtin and Scher, 1990) and composite materials transverse ply cracking Wittel et al. (2003).

The peridynamic (PD) theory, first proposed by Silling (2000), is a nonlocal formulation that allows to easily account for localization and fractures. Peridynamics has been successfully applied to the study of many problems, ranging from impact and/or penetration to crack propagation and bifurcation, dynamic fracture of membranes and mesoscale fracture modeling. Some noteworthy applications are shortly mentioned hereafter. Silling (2003) modeled the Kalthoff and Winkler (1988) experiment and correctly predicted the crack propagation angle in a notched plate made of maraging steel hit by a steel impactor. Later, Silling and Askari (2004) simulated the impact of a spherical, infinitely rigid projectile on an elastic-fragile thin disk. Demmie and Silling (2007) simulated structures under extreme loading conditions. Madenci and Oterkus (2016) developed a formulation to simulate plastic deformations based on von Mises yield criteria with isotropic hardening, while O'Grady and Foster (2014) addressed the bending of a Kirchhoff-Love plate.

Thermal deformations have been taken into account in order to predict crack paths due to prescribed thermal temperature histories in the body. For example, Kilic and Madenci (2009) predicted complex crack growth patterns plates after quenching. More recently Amani et al. (2016) simulated the Taylor-bar impact, accounting for temperature change due to plastic dissipation, but completely neglecting thermal conduction thanks to the extremely short time of the impact.

Besides structural mechanics, PD has been used to to develop complex models of multiphysics phenomena by e.g. Gerstle et al. (2007), where the thermal diffusion problem was reformulated for the first time using peridynamics. Later on, Bobaru and Duangpanya (2010; 2012) independently reformulated the heat equations in 1D and 2D, respectively. Their non-local solution tends to the local one as the coefficient that defines the material non-locality, addressed to as the horizon, tends to zero. Furthermore, Agwai (2011) proposed a PD formulation of the heat problem and a coupled formulation for the multiphysics thermo-mechanical problem and applied it to one dimensional elastic problems. Madenci and Oterkus (2014, Chapter 13) simulated two- and three-dimensional thermo-elastic problems. As a matter of fact, the PD reformulation of both the mechanical and the thermal problem presents some advantages, such as the possibility to use the same discretization to study both the mechanical and thermal transient problems and the capability of both models to take into account the onset of fracture surfaces during the simulation. However, none of the previous coupled thermo-mechanic papers did account for fractures; only very recently Oterkus and Madenci (2017) approached the coupled thermo-mechanic set of equations to simulate the thermal cracking of uranium dioxide fuel pellet.

This paper addresses the coupled PD thermo-mechanical problem in presence of evolving damages due to extreme thermal loading. Hence, the multiphysics thermo-mechanical problem is reformulated via PD, with the thermal-induced deformation affecting the mechanical response, and the onset of fracture surfaces preventing the transmission of heat. The formulation is implemented within the Open Source code Peridigm, see Park et al. (2012) for details.

The paper is organized as follows. The weakly coupled thermo-elastic peridynamics is briefly summarized in Sect. 2; due care is given to the definition of thermal boundary conditions, see Subsect. 2.2. The thermal code is validated in Sect. 3. Finally, two thermo-mechanical crack problems are dealt with in Sect. 4.

2. Weakly coupled thermo-elastic peridynamics

The PD formulation of the fully coupled thermo-mechanics has been developed by Gerstle et al. (2007), and later by Agwai (2011) and Madenci and Oterkus (2014, Chapter 13). In their work Madenci and Oterkus provided also a non-dimensionalization of the equations and some benchmark tests, such as a semi-infinite bar under thermal loading, thermo-elastic vibrations of a bar and a block of material under thermal loading. Agwai (2011) and Madenci and Oterkus (2014) solved the coupled problems without considering the possibility of an evolving damage in the domain of interest. The three-dimensional formulation here proposed, instead, follows a slightly different approach. The thermal problem is reformulated similarly to what proposed by Bobaru and Duangpanya (2010, 2012). Additionally, weak coupling between the thermal and the mechanical problem is assumed, so that a variation of temperature may introduce a thermal loading in the structure, but a change of the loading conditions cannot cause a variation of temperature. This assumption is generally valid for brittle-elastic materials, such as ceramics. This is the reason for which the case studies addressed in this paper simulate the behavior of alumina samples. A damage model based on the critical stretch criterion is introduced in the equations. This allows to properly account for material failure.

The following section briefly summarizes the weakly-coupled thermo-elastic peridynamic theory. It is by no means intended to be an exhaustive introduction to peridynamics; many results are reported without the corresponding proofs, that can be found in the cited references. Note also that even the notation developed throughout the years for the peridynamic theory is somewhat different from that of classical continuum mechanics. Notwithstanding our effort to be accurate and self-contained, the reader not accustomed to peridynamics is thus encouraged to refer to Silling et al. (2007), Silling (2010) and Silling and Lehoucq (2010) for a thorough introduction.

2.1. Governing equations

The peridynamic formulation that was first proposed is called bond-based peridynamics (BB-PD). It defines the density $\boldsymbol{f}$ of internal (bond) forces per unit of volume which are exchanged between different material points within a continuum. Thus, material points interact through bonds, with bond force densities depending only on the two interacting material points. Bonds forces are assumed to be non null only within a finite distance δ addressed as

horizon. The horizon is a material constant, and directly defines the material non-locality (see Ren et al. (2016) for an improved formulation with variable horizon). Note that $\boldsymbol{f}$, often referred as bond forces, are actually density of forces per unit of volume, i.e. forces per unit of volume squared. The force per unit of volume applied at any given point $\boldsymbol{x}$ is thus given by the integral, performed over the volume defined by the horizon, of the bond forces. The resulting equation of motion is thus

$$\rho(\boldsymbol{x})\ddot{\boldsymbol{u}}(\boldsymbol{x},t) = \int_{\mathfrak{S}_\delta} \boldsymbol{f}(\boldsymbol{u}(\boldsymbol{x}',t) - \boldsymbol{u}(\boldsymbol{x},t), \boldsymbol{x}' - \boldsymbol{x})\mathrm{d}V_{\boldsymbol{x}'} + \boldsymbol{b}(\boldsymbol{x},t) \qquad (1)$$

with ρ the material density, $\boldsymbol{u}$ the displacement, $\boldsymbol{b}$ the applied forces per unit of volume and $\mathfrak{S}_\delta$ the sphere of radius δ centered in $\boldsymbol{x}$; $\mathrm{d}V_{\boldsymbol{x}'}$ means that the integral is performed over $\mathfrak{S}_\delta$ by keeping $\boldsymbol{x}$ fixed and varying $\boldsymbol{x}'$. The relative position of two points in the reference configuration is often referred as $\boldsymbol{\xi} = \boldsymbol{x}' - \boldsymbol{x}$; their relative displacement is $\boldsymbol{\eta} = \boldsymbol{u}' - \boldsymbol{u}$, so that their relative position in the deformed configuration is $\boldsymbol{y}' - \boldsymbol{y} = \boldsymbol{\xi} + \boldsymbol{\eta}$, cfr. Fig. 1. Silling (2000) showed that, for a microelastic brittle BB-PD material, bond forces are co-axial with the deformed configuration relative position $\boldsymbol{y}' - \boldsymbol{y} = \boldsymbol{\xi} + \boldsymbol{\eta}$, and their magnitude is a function of the relative distance in the reference and deformed configurations, $\|\boldsymbol{\xi}\|$ and $\|\boldsymbol{\xi} + \boldsymbol{\eta}\|$. Having bond forces co-axial with the relative position of the interacting points guaranties that the balance of angular momentum is automatically satisfied, see e.g. Silling et al. (2007) for details.

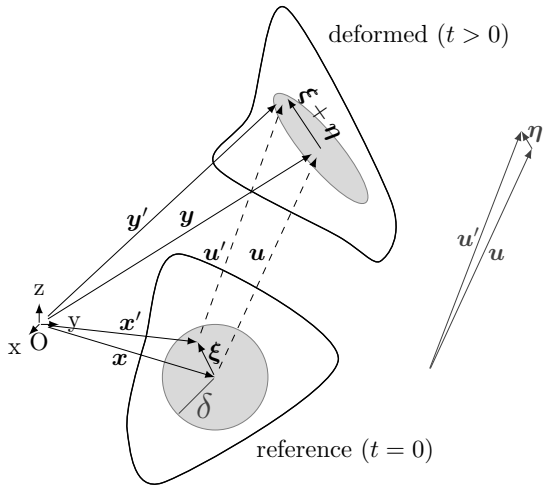

Figure 1: Kinematics in the reference and deformed configurations for a PD continuum.

Although successful, bond-based peridynamics suffers from some serious shortcomings; among them, the Poisson's ratio of any isotropic elastic material is fixed and equal to $\nu = 1/3$ for two-dimensional problems and $\nu = 1/4$ for three-dimensional problems, see Silling and Askari (2005). More importantly, it is difficult to relate bond forces to constitutive laws developed in classical mechanics, i.e. based on the notion of contact forces. To overcome these – and other – limitations Silling et al. (2007) proposed the so-called state-based peridynamics (SB-PD). To do that, they introduced the concept of state. A state $\underline{\boldsymbol{A}}$ of order m is a tensor function of order m, function of the position $\boldsymbol{\xi}$ inside a sphere of radius δ centered at the origin. The somewhat unusual notation $\underline{\boldsymbol{A}}\langle\boldsymbol{\xi}\rangle$ stands for tensor that is the image of $\boldsymbol{\xi}$ under the state $\underline{\boldsymbol{A}}$. A state field is a state-valued function of position $\boldsymbol{x}$ and time t. The location and time at which a state field is evaluated are in square brackets to distinguish them from $\boldsymbol{\xi}$. Thus, $\underline{\boldsymbol{A}}[\boldsymbol{x}, t]\langle\boldsymbol{x}' - \boldsymbol{x}\rangle$ stands for a state field, evaluated at the reference position $\boldsymbol{x}$ and time t, for $\boldsymbol{\xi} = \boldsymbol{x}' - \boldsymbol{x}$. The following states are introduced:

$$
\begin{aligned}
\text{the reference position state: } & \underline{\boldsymbol{X}}[\boldsymbol{x}, t]\langle\boldsymbol{x}' - \boldsymbol{x}\rangle = \boldsymbol{x}' - \boldsymbol{x}, \\
\text{the displacement state: } & \underline{\boldsymbol{U}}[\boldsymbol{x}, t]\langle\boldsymbol{x}' - \boldsymbol{x}\rangle = \boldsymbol{u}' - \boldsymbol{u}, \\
\text{the deformed position state: } & \underline{\boldsymbol{Y}}[\boldsymbol{x}, t]\langle\boldsymbol{x}' - \boldsymbol{x}\rangle = \boldsymbol{y}' - \boldsymbol{y}.
\end{aligned}
$$

Departing from Eq. 1, the state-based peridynamic equation of motion reads

$$\rho(\boldsymbol{x})\frac{\partial^2 \boldsymbol{u}}{\partial t^2}(\boldsymbol{x},t) = \int_{\mathfrak{S}_\delta} \left(\underline{\boldsymbol{T}}[\boldsymbol{x},t]\langle \boldsymbol{x}'-\boldsymbol{x}\rangle - \underline{\boldsymbol{T}}[\boldsymbol{x}',t]\langle \boldsymbol{x}-\boldsymbol{x}'\rangle\right) \mathrm{d}V_{\boldsymbol{x}'} + \boldsymbol{b}(\boldsymbol{x},t), \quad (2)$$

where $\underline{\boldsymbol{T}}$ is called the force vector state field. This equation reduces to Eq. 1 whenever $\underline{\boldsymbol{T}}[\boldsymbol{x}',t]\langle \boldsymbol{x}-\boldsymbol{x}'\rangle = -\underline{\boldsymbol{T}}[\boldsymbol{x},t]\langle \boldsymbol{x}'-\boldsymbol{x}\rangle$. However, in general, $\underline{\boldsymbol{T}}[\boldsymbol{x}',t]\langle \boldsymbol{x}-\boldsymbol{x}'\rangle \neq -\underline{\boldsymbol{T}}[\boldsymbol{x},t]\langle \boldsymbol{x}'-\boldsymbol{x}\rangle$, i.e. force densities are not pairwise equilibrated. This is possible because $\underline{\boldsymbol{T}}[\boldsymbol{x},t]\langle \boldsymbol{x}'-\boldsymbol{x}\rangle$ is assumed to depend on all the points within the horizon of $\boldsymbol{x}$, although this is not made explicit by the notation. The bond-based peridynamics assumes, instead, that $\underline{\boldsymbol{T}}[\boldsymbol{x},t]\langle \boldsymbol{x}'-\boldsymbol{x}\rangle$ does depend only on $\boldsymbol{x}$ and $\boldsymbol{x}'$, and this implies that $\underline{\boldsymbol{T}}[\boldsymbol{x}',t]\langle \boldsymbol{x}-\boldsymbol{x}'\rangle = -\underline{\boldsymbol{T}}[\boldsymbol{x},t]\langle \boldsymbol{x}'-\boldsymbol{x}\rangle$.

A material for which the force vector state field is co-axial with $\underline{\boldsymbol{Y}}$ is called an ordinary material. A material for which the force vector state field is not co-axial with $\underline{\boldsymbol{Y}}$ is called an non-ordinary material, see e.g. Warren et al. (2009). Figure 2 compares these three different models. Note that the balance of angular momentum is identically satisfied for ordinary materials; on the contrary, it is not automatically satisfied for non–ordinary state-based materials, and this introduces a restriction on the form of $\underline{\boldsymbol{T}}$, see again Silling et al. (2007) and Silling and Lehoucq (2010) for details. To be objective, the force vector state field $\boldsymbol{T}$ should transform like $\underline{\boldsymbol{Y}}$ under rigid body rotation. That is, $\underline{\boldsymbol{T}}(\boldsymbol{Q}\underline{\boldsymbol{Y}}) = \boldsymbol{Q}\underline{\boldsymbol{T}}(\underline{\boldsymbol{Y}})$ for any $\boldsymbol{Q} \in \mathrm{SO}(3)$. A sufficient condition for objectivity of ordinary materials is that $\underline{\boldsymbol{T}} = \frac{\underline{\boldsymbol{Y}}}{\|\underline{\boldsymbol{Y}}\|}\underline{t}(\|\underline{\boldsymbol{Y}}\|)$, where $\underline{t}(\|\underline{\boldsymbol{Y}}\|)$ is a scalar state function of $\|\underline{\boldsymbol{Y}}\|$.

As shown e.g. by Silling et al. (2007), Silling and Lehoucq (2010) and Tupek and Radovitzky (2014) it is possible calibrate state-based material models in such a way that they give the same results, for a homogeneous state of deformation, that would be obtained with a classical, stress-based constitutive law.

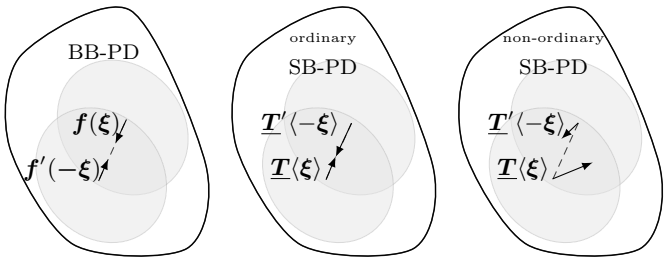

Figure 2: BB-PD: Pairwise equilibrated force densities; SB-PD: Ordinary unequal aligned force densities, NOSB-PD: arbitrarily oriented force densities.

Material model

The material model considered here is the Linear Peridynamic Solid (LPS) introduced by Silling et al. (2007).

Define the weighted volume as

$$\mathcal{M}[\boldsymbol{x}] = \int_{\mathfrak{S}_\delta} \underline{\omega}\langle\boldsymbol{\xi}\rangle \, \underline{x}\langle\boldsymbol{\xi}\rangle \, \underline{x}\langle\boldsymbol{\xi}\rangle \, \mathrm{d}V_{\boldsymbol{x}'}, \tag{3}$$

where $\underline{x}\langle\xi\rangle = \|\underline{\boldsymbol{X}}\| = \|\boldsymbol{\xi}\|$ and $\underline{\omega}\langle\xi\rangle$ is a scalar influence function that allows to weight differently the state of points at different $\boldsymbol{\xi}$; note again that $\mathrm{d}V_{\boldsymbol{x}'}$ means that the integral is performed over $\mathfrak{S}_\delta$ by keeping $\boldsymbol{x}$ fixed and varying $\boldsymbol{x}'$. Seleson and Parks (2011) investigated the effects on the structural response of choosing different influence functions. Define the extension scalar state as

$$\underline{e}[\boldsymbol{x}, t]\langle\boldsymbol{\xi}\rangle = \underline{y} - \underline{x} = \|\underline{\boldsymbol{Y}}\| - \|\underline{\boldsymbol{X}}\|. \tag{4}$$

The dilatational component of the extension scalar state is defined as

$$\theta = \frac{3}{\mathcal{M}} \int_{\mathfrak{S}_\delta} \underline{\omega}\langle\xi\rangle \, \underline{x}\langle\xi\rangle \, \underline{e}\langle\xi\rangle \, \mathrm{d}V_{\boldsymbol{x}'}, \tag{5}$$

while the deviatoric component is

$$\underline{e}^d = \underline{e} - \frac{\theta}{3}\underline{x}. \tag{6}$$

The LPS is an ordinary material, thus only force states co-axial with the relative position in the deformed configuration are considered. After defining

the deformed direction vector state, $\underline{\boldsymbol{M}}\langle\boldsymbol{\xi}\rangle$,

$$\underline{\boldsymbol{M}}\langle\boldsymbol{\xi}\rangle = \begin{cases} \dfrac{\boldsymbol{\xi}+\boldsymbol{\eta}}{\|\boldsymbol{\xi}+\boldsymbol{\eta}\|} & \text{if } \|\boldsymbol{\xi}+\boldsymbol{\eta}\| \neq 0 \\ \mathbf{0} & \text{otherwise} \end{cases}. \tag{7}$$

the force state for a three dimensional thermoelastic LPS material with a thermal contribute can be written as

$$\underline{\boldsymbol{T}}[\boldsymbol{x},t]\langle\boldsymbol{\xi}\rangle = \frac{\underline{\omega}\langle\boldsymbol{\xi}\rangle\underline{\boldsymbol{M}}\langle\boldsymbol{\xi}\rangle}{\mathcal{M}}\Big(3K\theta\|\boldsymbol{\xi}\| + 15\mu\big(\underline{e}^d\langle\boldsymbol{\xi}\rangle - \alpha(\Theta-\Theta_{\boldsymbol{\sigma}=\mathbf{0}})\|\boldsymbol{\xi}\|\big)\Big), \tag{8}$$

where K is the bulk modulus, μ is the shear modulus and α is the thermal expansion coefficient. In the following we will consider only constant influence functions, $\underline{\omega}\langle\xi\rangle = 1$. Note that the coefficients of Eq. 8 would be different for two-dimensional problems, see e.g. Ren et al. (2016) for details.

Thermal problem

The reformulation of the thermal diffusion problem is proposed by means of the BB-PD: the heat flux per unit volume between two points $\boldsymbol{x}$ and $\boldsymbol{x}'$ is assumed to depend only on the temperature in $\boldsymbol{x}$ and $\boldsymbol{x}'$. The first BB-PD formulation of the thermal problem was proposed by Bubaru and Dunagpanya (2010; 2012). Later, Agwai (2011, Chapter 12) and Madenci and Oterkus (2014, Chapter 12) introduced a slightly different form of the BB-PD thermal problem, based on energetic considerations.

The BB-PD form of the thermal diffusion problem can be written, after defining the pairwise heat exchanged per unit of volume squared f_h, as

$$\rho(\boldsymbol{x})c_v\frac{\partial\Theta}{\partial t}(\boldsymbol{x},t) = \int_{\mathfrak{S}_\delta} f_h\big(\Theta(\boldsymbol{x}',t)-\Theta(\boldsymbol{x},t),\boldsymbol{x}'(t)-\boldsymbol{x}(t),t\big)\,\mathrm{d}V_{\boldsymbol{x}'} + h_s(\boldsymbol{x},t) \qquad \forall\,\boldsymbol{x}\in\mathfrak{R}, \quad \wedge \quad \forall\, t>0, \tag{9}$$

where ρ is the material density, c_v is the specific heat and h_s is an internal heat source. The pairwise exchanged heat density is found to be

$$f_h\big(\Theta'(t)-\Theta(t),\boldsymbol{x}'(t)-\boldsymbol{x}(t),t\big) = \kappa\frac{\Theta(\boldsymbol{x}',t)-\Theta(\boldsymbol{x},t)}{\|\boldsymbol{x}'(t)-\boldsymbol{x}(t)\|}, \tag{10}$$

where $\Theta'(t) = \Theta(\boldsymbol{x}', t)$, $\Theta(t) = \Theta(\boldsymbol{x}, t)$; the coefficient κ is named micro-conductivity, and is computed by equating the local and non-local thermal potential. The microconductivity depends on the classical thermal conductivity, on the horizon δ and on the problem dimensions (i.e. it is different for 1D, 2D or 3D problems).

Critical stretch damage model

The damage model is introduced to allow bonds to break within the body. A bond breakage is an irreversible phenomenon. When a given bond breaks the interactions between particles are suddenly interrupted. After defining the bond stretch as

$$s(\|\boldsymbol{\xi}\|, \|\boldsymbol{\xi} + \boldsymbol{\eta}\|) = \frac{\|\boldsymbol{\xi} + \boldsymbol{\eta}\| - \|\boldsymbol{\xi}\|}{\|\boldsymbol{\xi}\|}, \tag{11}$$

a bond is assumed to be broken when the stretch becomes larger than the so-called critical stretch s_c. The critical stretch depends on the fracture energy, G_c, i.e. on the energy per unit length necessary to create a new free surface. Madenci and Oterkus (2014, Chapter 12) have found the critical stretch expression for 2D and for 3D problems:

$$s_{c_{2D}} = \sqrt{\frac{G_c}{\left(\frac{6}{\pi}\mu + \frac{16}{9\pi^2}\big(K - 2\mu\big)\right)\delta}}, \tag{12}$$

$$s_{c_{3D}} = \sqrt{\frac{G_c}{\left(3\mu + \big(\frac{3}{4}\big)^4\big(K - \frac{5}{3}\mu\big)\right)\delta}}. \tag{13}$$

The boolean state $\phi[\boldsymbol{x}, t]\langle\boldsymbol{\xi}\rangle$ is equal to zero if the bond is broken, otherwise it is equal to one:

$$\phi[\boldsymbol{x}, t]\langle\boldsymbol{\xi}\rangle = \begin{cases} 1 & \text{if } s < s_c \\ 0 & \text{if } s \geq s_c \end{cases}. \tag{14}$$

The complete PD form of the multiphysics thermo-mechanical problem with damage becomes:

$$\begin{cases} \rho(\boldsymbol{x})\,\ddot{u}(\boldsymbol{x},t) & = \int_{\mathfrak{S}_\delta} \phi[\boldsymbol{x},t]\langle\boldsymbol{\xi}\rangle \big(\underline{\boldsymbol{T}}[\boldsymbol{x},t]\langle\boldsymbol{\xi}\rangle - \underline{\boldsymbol{T}}[\boldsymbol{x}',t]\langle-\boldsymbol{\xi}\rangle\big)\,\mathrm{d}V_{\boldsymbol{x}'} + \boldsymbol{b}(\boldsymbol{x},t) \\ \rho(\boldsymbol{x})\,c_v\dot{\Theta}(\boldsymbol{x},t) & = \int_{\mathfrak{S}_\delta} \phi[\boldsymbol{x},t]\langle\boldsymbol{\xi}\rangle f_h\big(\Theta(\boldsymbol{x}',t) - \Theta(\boldsymbol{x},t), \boldsymbol{\xi}(t), t\big)\,\mathrm{d}V_{\boldsymbol{x}'} + h_s(\boldsymbol{x},t) \end{cases}. \tag{15}$$

The global damage of the material point $\boldsymbol{x}$, namely $\Phi(\boldsymbol{x},t)$, is defined as

$$\Phi(\boldsymbol{x},t) = 1 - \frac{\int_{\mathfrak{S}_\delta} \phi\,\mathrm{d}V_{\boldsymbol{x}'}}{\int_{\mathfrak{S}_\delta}\mathrm{d}V_{\boldsymbol{x}'}}. \tag{16}$$

Thus, $\Phi(\boldsymbol{x},t) = 1$ if all the bonds at a point $\boldsymbol{x}$ are broken.

2.2. Thermal boundary conditions

Prescribed temperature

Prescribed temperature, an essential boundary condition (BC), can be enforced by simply assigning the correct value to the boundary points, as shown by Bobaru and Duangpanya (2010).

$$\Theta(\boldsymbol{x}_{BC},t) = \Theta_{\boldsymbol{x}_{BC}}(t). \tag{17}$$

Prescribed heat flux

Natural BCs need a special treatment in peridynamics, as first shown by Silling (2000) for the mechanical problem. This is because the stress at a point does depend on the state of its whole family. Following Silling's approach, Madenci and Oterkus (2014, Chapter 12) proposed an analogue procedure for thermal problems BCs. The same approach is adopted in the present study, too. Natural and mixed BCs in peridynamics can be enforced by adding external volume forces $\boldsymbol{b}(\boldsymbol{x},t)$ for the mechanical problem, and internal heat sources $h_s(\boldsymbol{x},t)$ for thermal problem. These volume forces and heat sources need to transmit to the body the same power that would be introduced by the corresponding boundary condition of the local theory. Note that PD BCs are actually imposed over the volume represented by the family of points of the external surface and not over the points of the surface alone. Nonetheless, if the horizon tends to zero, then the PD BC converges to the local BC.

A prescribed heat flux, i.e. a Neumann BC, is introduced in the solid through an internal heat source. We denote with $\mathcal{S}_{\boldsymbol{q}}$ the boundary surface with a prescribed heat flux per unit of surface $\boldsymbol{q}$, with $\boldsymbol{n}$ the unit normal to the surface and with $V_{\boldsymbol{q}}$ the volume of the boundary particles on which the prescribed internal heat sources have to be introduced. Eq. 18 must be satisfied in order to compute the equivalent volume heat source $h_{\boldsymbol{q}}$:

$$h_{\boldsymbol{q}} V_{\boldsymbol{q}} = -\int_{\mathcal{S}_{\boldsymbol{q}}} \boldsymbol{q} \cdot \boldsymbol{n} \, \mathrm{d}\mathcal{S}. \tag{18}$$

This means that, assuming constant heat flux $\boldsymbol{q}$ and a planar surface $\mathcal{S}_{\boldsymbol{q}}$ one has

$$h_{\boldsymbol{q}} = \frac{-\int_{\mathcal{S}_{\boldsymbol{q}}} \boldsymbol{q} \cdot \boldsymbol{n} \, \mathrm{d}\mathcal{S}}{V_{\boldsymbol{q}}} = -\frac{\boldsymbol{q} \cdot \boldsymbol{n} \, \mathcal{S}_{\boldsymbol{q}}}{\mathcal{S}_{\boldsymbol{q}} \Delta} = -\frac{\boldsymbol{q} \cdot \boldsymbol{n}}{\Delta}, \tag{19}$$

where Δ is the distance from the boundary such that $V_{\boldsymbol{q}} = \mathcal{S}_{\boldsymbol{q}} \Delta$.

Convection

The convection BC is defined as

$$\mathbf{q}(\boldsymbol{x}, t) \cdot \mathbf{n} = h\big(\Theta(\boldsymbol{x}_B, t) - \Theta_\infty\big), \tag{20}$$

where h and Θ_∞ are the convective heat transfer coefficient and the temperature of the fluid surrounding the domain, while $\Theta(\boldsymbol{x}_B, t)$ is the domain boundary temperature. Dividing Eq. 20 by Δ allows to compute the internal heat source that is necessary to enforce the convection BC via peridynamics

$$h_h(\boldsymbol{x}, t) = h\frac{\big(\Theta_\infty - \Theta(\boldsymbol{x}_B, t)\big)}{\Delta}. \tag{21}$$

2.3. Numerical discretization

It is customary to search an approximated solution of peridynamics equations by direct collocation. To this end, the equations of motion are written at a finite number of points, often referred to as particles in the peridynamics literature. Note that this nomenclature is somewhat misleading, at least in our opinion, because these particles are not actually discrete masses, as would be the case with approaches based on mass point mechanics, such as spring network models (see e.g. Curtin and Scher, 1990) or nearest-neighbor methods (see e.g. Hayakawa, 1994a). Rather, they are the points at which the equations are enforced. Equation 15 is thus collocated at the particle

location $\boldsymbol{x}_{(i)}$. The integrals of Eq. 15 are approximated by assigning to each particle a finite volume $\Delta V_{(i)}$. The set of particles $\boldsymbol{x}_{(j)}$ belonging to the family of a given particle $\boldsymbol{x}_{(i)}$ is called $P_{(i)}$:

$$P_{(i)} = \{\boldsymbol{x}_{(j)} \neq \boldsymbol{x}_{(i)} \,:\, \|\boldsymbol{x}_{(j)} - \boldsymbol{x}_{(i)}\| \leq \delta\} \tag{22}$$

Thus, the semi-discrete PD thermo-mechanical balance equations for particle $\boldsymbol{x}_{(i)}$ can be approximated as

$$\begin{cases} \rho_{(i)}\ddot{\boldsymbol{u}}_{(i)}(t) & = \sum\limits_{\boldsymbol{x}_{(j)} \in P_{(i)}} \phi_{ij} \boldsymbol{f}\big(\boldsymbol{x}_{(i)}, \boldsymbol{x}_{(j)}\big) \Delta V_{(j)} + \boldsymbol{b}_{(i)}(t) \\ \rho_{(i)} c_{v(i)} \dot{\Theta}_{(i)}(t) & = \kappa \sum\limits_{\boldsymbol{x}_{(j)} \in P_{(i)}} \phi_{ij} \left\{ \frac{\Theta(\boldsymbol{x}_{(j)},t) - \Theta(\boldsymbol{x}_{(i)},t)}{\|\boldsymbol{x}_{(j)} - \boldsymbol{x}_{(i)}\|} \right\} \Delta V_{(j)} + h_{s(i)}(t) \end{cases}, \tag{23}$$

where $\boldsymbol{f}\big(\boldsymbol{x}_{(i)}, \boldsymbol{x}_{(j)}\big) = \underline{\boldsymbol{T}}[\boldsymbol{x}_{(j)}, t]\langle \boldsymbol{x}_{(j)} - \boldsymbol{x}_{(i)} \rangle - \underline{\boldsymbol{T}}[\boldsymbol{x}_{(i)}, t]\langle \boldsymbol{x}_{(i)} - \boldsymbol{x}_{(j)} \rangle$, $\phi_{ij} = \phi[\boldsymbol{x}_{(i)}, t]\langle \boldsymbol{x}_{(j)} - \boldsymbol{x}_{(i)} \rangle$ and the volume integral is approximated by assuming that all the finite volume $\Delta V_{(j)}$ of particle $\boldsymbol{x}_{(j)}$ does belong to the family of particle $\boldsymbol{x}_{(i)}$. Note, again, that the resulting set of discrete equations may resemble, at a first glance, what one would obtain with mass point mechanics. The derivation, however, is completely different.

2.4. Multirate integration

Explicit integrators are a good choice to integrate the PD thermo-mechanical problem because they are well suited to deal with large displacements and evolving discontinuities. However, Von Neumann stability analyses show that the ratio between the thermal problem critical time step, Δt_{cr}^{TH}, and the mechanical critical time step, Δt_{cr}^{ME}, can reach values as large as 1e6. As a matter of fact, the typical time scales for elasto-dynamic phenomena do depend on the propagation velocity of stress waves in the material, hence on the speed of sound in the material; the time scales of thermal problems, instead, are much larger, since they depend on the thermal diffusivity of the material. For this reason the discretized problem cannot be based on a single time step, since both problems have to be solved towards their natural evolution velocity. Doing otherwise, i.e. using a single time step for the mechanical and thermal problem still guaranteeing the overall numerical stability, could lead to a temperature increment within a time step smaller than the machine epsilon multiplied by the current temperature. In other words, the loss of precision for the temperature could – and has been verified that it would –

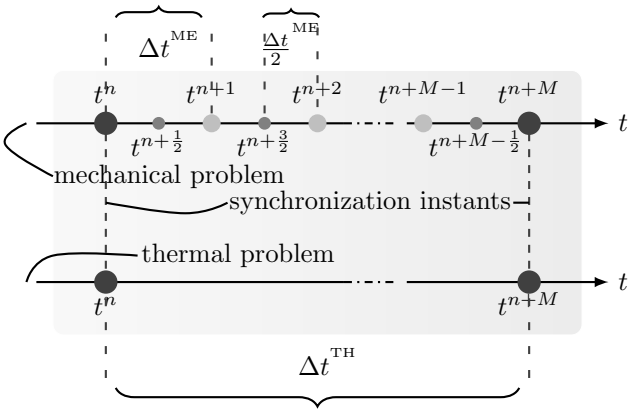

Figure 3: Multirate integration scheme.

be so dramatic that the temperature would keep unchanged throughout the entire simulation. This suggests to adopt a multirate integrator (for further details about multirate integrators, the reader should refer to Gear and Wells (1984), Savcenco and Mattheij (2010) and Seny et al. (2014)), that is well suited for multiphysics problems characterized by substantially different time scales.

The Velocity Verlet integration scheme is used for the mechanical problem, while the Forward Euler is preferred for the thermal problem. The thermal solution is updated each M time steps and it is considered to remain constant between $\Delta t^{(n)}$ and $\Delta t^{(n+M)}$, as schematically shown in Fig. 3. The Alg. 1 better explains the adopted multirate integration technique.

3. Numerical implementation and validation of peridynamic thermal diffusion

The peridynamic thermal transient solution, for a prescribed discretization and horizon, is compared with the classical solution. For the convergence tests, the non-locality parameter m is defined as the ratio of the horizon δ and the distance between two material particles, Δx, namely $m = \delta/\Delta x$. The convergence is investigated by considering the definitions given by Bobaru et al. (2009), were the concepts of m-convergence and δ-convergence were introduced. As regards the m-convergence, the horizon δ is kept constant and the non-locality parameter tends to infinite, $m \to \infty$ (cfr.Fig. 4a). In this case, the numeric peridynamic solution has to converge to the exact non-local peridynamic solution for the prescribed δ. For the δ-convergence,

Algorithm 1 Multirate integration scheme

Input: Initialize problem variables and estimate critical time steps

$n = 0$ // Time step indexing: $n \in 1 : \mathcal{N}$

$t = 0$ // Initialize time variable

Δt_{cr}^{ME} // Critical time step -mechanical problem-

Δt_{cr}^{TH} // Critical time step -thermal problem-

$M = \frac{\mathcal{N}}{N}$ // Synchronization interval between the problems

$\mathbf{u}, \mathbf{a} = \mathbf{0}$ // Initialize kinematic variables

Reading material properties

Apply the Initial Conditions

Output: Updated variables

$\mathbf{u}^{n+1}$, $\mathbf{v}^{n+1}$, $\mathbf{a}^{n+1}$, $\mathbf{f}^{n+1}$ // Mechanical pb. to be solved at each time step

Θ^{n+M}, $\dot{Q}^{n+M}$ // Thermal pb. to be solved every M time steps

procedure MULTIRATE INTEGRATOR

  for $n = 1,\mathcal{N}$ **do**

    $t^{(n+1)} = t^{(n)} + \Delta t^{ME}$ // Update the time step.

    $t^{(n+\frac{1}{2})} = \frac{1}{2}\left(t^{(n)} + t^{(n+1)}\right)$ // Evaluate the mid step

    $\mathbf{v}^{(n+\frac{1}{2})} = \mathbf{v}^{(n)} + \left(t^{(n+\frac{1}{2})} - t^{(n)}\right)\mathbf{a}^{(n)}$ // *Velocity Verlet* I

    Apply velocity BCs at the mid step

    $\mathbf{u}^{(n+1)} = \mathbf{u}^{(n)} + \Delta t^{ME}\mathbf{v}^{(n+\frac{1}{2})}$ // *Velocity Verlet* II

    Apply displacements BCs at $t^{(n+1)}$

    if $\frac{n}{M}$ **is** integer **then**

      Compute $\int_{\mathfrak{S}_\delta} f_h^{(n+1)}\,\mathrm{d}V_{\boldsymbol{x}'}$ // Compute heat exchanged

      $\Theta^{(n+1)} = \Theta^{(n)} + \frac{\Delta t^{TH}}{\rho c_v}\left(\int_{\mathfrak{S}_\delta} f_h^{(n+1)}\,\mathrm{d}V_{\boldsymbol{x}'} + h_s\right)$ // *forward Euler*

      Apply Thermal BCs at $t^{(n+1)}$ // See Sec. 2.2

    end if

    Compute $\mathbf{f}_{int}^{(n+1)}$ // Compute internal force density

    Eventually, compute $\mathbf{f}_{cont}^{(n+1)}$ // Compute contact force density

    $\mathbf{f}^{(n+1)} = \mathbf{f}_{int}^{(n+1)} + \mathbf{f}_{cont}^{(n+1)} + \mathbf{b}^{(n+1)}$ // Compute force density

    $\mathbf{a}^{(n+1)} = \mathrm{diag}\left\{\rho\right\}^{-1}\mathbf{f}^{(n+1)}$ // Compute acceleration

    $\mathbf{v}^{(n+1)} = \mathbf{v}^{(n+\frac{1}{2})} + \frac{\Delta t}{2}^{ME}\mathbf{a}^{(n+1)}$ // *Velocity Verlet* III

    Stability check (energy balance)

  end for

end procedure

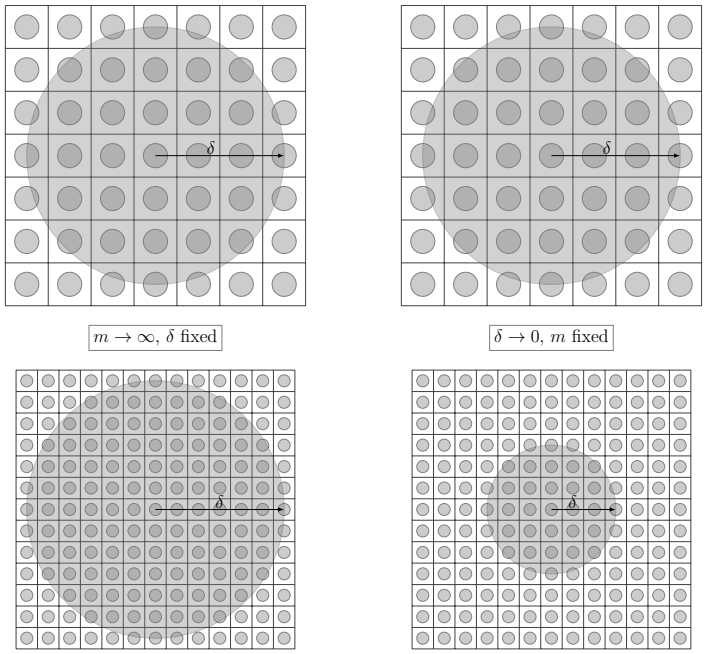

(a) m-convergence scheme. (b) δ-convergence scheme.

Figure 4: Peridynamic convergence: δ-convergence and m-convergence for a regular 2D square mesh.

instead, m is kept fixed while the horizon tends to zero, $\delta \to 0$ (cfr. Fig. 4b). In this way the non-locality is gradually reduced and the non-local solution must approximate the local one, i.e. the degenerated case $\delta = 0$.

3.1. 1D test case

In this 1D validation study a bar with mixed Dirichlet-Neumann boundary conditions is considered. The bar has length $X = 1$ m, thermal diffusivity $\gamma = 0.13$ W m^{-2} s^{-1} and its initial temperature is 0 °C for $0 < x \leq X/2$ and 60 °C for $x/2 < x \leq X$. The classical problem is defined by Eqs. (24-27):

$$\frac{1}{\gamma}\frac{\partial\Theta(x,t)}{\partial t} = \frac{\partial^2\Theta(x,t)}{\partial x^2}, \tag{24}$$

$$\Theta(0,t) = 100, \quad \forall t \geq 0, \tag{25}$$

$$\frac{\partial\Theta(X,t)}{\partial x} = 0, \quad \forall t \geq 0, \tag{26}$$

$$\Theta(x,0) = \begin{cases} 0 & \forall\, 0 < x \leq X/2, \\ 60 & \forall\, X/2 < x \leq X. \end{cases} \tag{27}$$

The classical solution is obtained numerically using the finite difference BCTS scheme (backward in time, central in space) of Eq. 28. The bar is discretized using 200 nodes.

$$\frac{\Theta(x_{(i)},t^{(j+1)}) - \Theta(x_{(i)},t^{(j)})}{\Delta t} = \\ \frac{1}{\gamma}\frac{\Theta(x_{(i+1)},t^{(j+1)}) - 2\Theta(x_{(i)},t^{(j+1)}) + \Theta(x_{(i-1)},t^{(j+1)})}{\Delta x^2} + \mathcal{O}(\Delta t, \Delta x^2). \tag{28}$$

For the peridynamic discretization 100 material particles are used, and the horizon is chosen to be $\delta = 3\,X/101 \simeq 0.0297\,X$, thus $m = \delta/\Delta x = 3$. The results for $t = 0.88$ s and $t = 3.60$ s are plotted in Fig. (5), with the finite difference and PD solutions practically coincident.

m-convergence

For the m-convergence test, four fixed values of δ ($\delta_1 = 0.015$ m, $\delta_2 = 0.030$ m, $\delta_3 = 0.060$ m and $\delta_4 = 0.075$ m) are considered in order to verify that the non-local solution tends to the local one as the horizon approaches zero, while the non-locality parameter tends to infinite. As the non-locality parameter increases, the smaller the horizon is, the slower the PD solution should move from the local one. This behavior is observed in Fig. 6, where the mean temperature of the bar is plotted for $t = 3.6$ s. For $m \simeq 3$ all the curves intersect, thus the PD solution matches the local one, independently from the discretization.

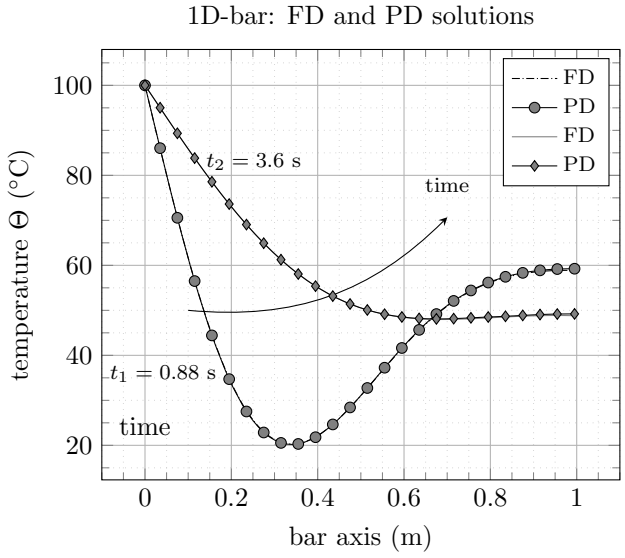

Figure 5: Comparison between the classical solution approximated with the finite differences method and the PD solution for two different instants of time. The horizon size is $\delta = 3\Delta x$.

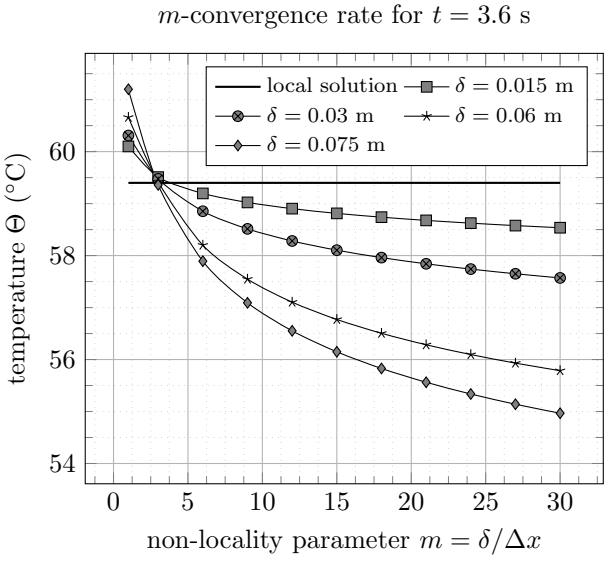

Figure 6: m-convergence diagram for $t = 3.6$ s. Observe that all the curves intersect the local solution for $m \simeq 3$.

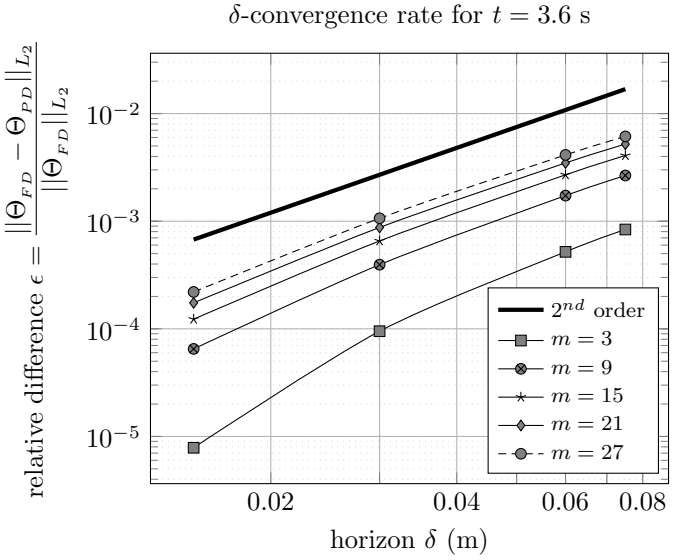

Figure 7: δ-convergence rate. At least second order convergence rate to the local solution is observed for all the values of m.

δ-convergence

To perform the δ-convergence test, the values 0.015 m $\leq \delta \leq$ 0.075 m are used. The tests are performed for five different choices of the non-locality parameter, $m = 3$, $m = 9$, $m = 15$, $m = 21$, $m = 27$. The δ-convergence rates are obtained by defining the relative difference between the local and the PD solution, i.e.:

$$\epsilon = \frac{||\Theta_{FD} - \Theta_{PD}||_{L_2}}{||\Theta_{FD}||_{L_2}}. \tag{29}$$

Following Bobaru and Duangpanya (2010; 2012) ϵ is called relative difference and not relative error since it is not relative to the unknown analytical peridynamic solution. The results are shown in Fig. 7 and compared with the thick continuous curve representing the 2$^{\text{nd}}$order of convergence. As observed, for $m = 3$ the convergence rate is apparently higher than 2. For this reason and because of the results of m-convergence tests, the value of m chosen for the thermo-mechanical problems is 3.

3.2. 2D test case

For the 2D validation study we consider a plate with dimensions of $X =$ 0.05 m (length), $Y = 0.01$ m (height) and $Z = 0.001$ m (thickness), and

thermal diffusivity $\gamma = 0.1$ Wm^{-2} s^{-1}. The plate is subjected to a prescribed temperature $\Theta_{BC} = 100$ °C on its boundaries. Its initial temperature is $\Theta_0 = 0$ °C. The classical formulation of the problem reads:

$$\frac{1}{\gamma}\frac{\partial\Theta(x,y,t)}{\partial t} = \frac{\partial^2\Theta(x,y,t)}{\partial x^2} + \frac{\partial^2\Theta(x,y,t)}{\partial y^2}, \tag{30}$$

$$\Theta(0,y,t) = \Theta(X,y,t) = 100, \quad \forall t > 0, \tag{31}$$

$$\Theta(x,0,t) = \Theta(x,Y,t) = 100, \quad \forall t < 0, \tag{32}$$

$$\Theta(x,y,0) = 0. \tag{33}$$

Again, the classical solution is obtained numerically through the BCTS finite differences method of Eq. 34. The plate is discretized using 350 nodes along the x axis and 70 nodes along the y axis.

$$\frac{\Theta(x_{(i)},y_{(k)},t^{(j+1)}) - \Theta(x_{(i)},y_{(k)},t^{(j)})}{\Delta t} = \frac{1}{\gamma}\left(\frac{\Theta(x_{(i+1)},y_{(k)},t^{(j+1)}) - 2\Theta(x_{(i)},y_{(k)},t^{(j+1)}) + \Theta(x_{(i-1)},y_{(k)},t^{(j+1)})}{\Delta x^2} + \frac{\Theta(x_{(i)},y_{(k+1)},t^{(j+1)}) - 2\Theta(x_{(i)},y_{(k)},t^{(j+1)}) + \Theta(x_{(i)},y_{(k-1)},t^{(j+1)})}{\Delta y^2}\right) + \mathcal{O}(\Delta t, \Delta x^2, \Delta y^2) \tag{34}$$

The PD problem is discretized into $\mathcal{N}$ =24500 material points, each one having area $\Delta x \times \Delta y$, where $\Delta x = X/349$ is the spacing between material points along the x axis and $\Delta y = Y/69$ is the spacing between material points along the y axis. From Subsec. 3.1 the optimal non-locality parameter to approximate the local solution is $m = 3$, hence $\delta = 3 \cdot \max(\Delta x, \Delta y)$ is expected to be the optimal horizon size. Recall that in a PD model the non-local interactions are not negiglible only within the horizon, as schematically shown in Fig. 8, thus in a 2D problem the family of a generic point $x_{(i)}$ is enclosed inside a circle of radius δ.

The classical and the peridynamic solution are compared in Fig. 9, where the plate half span temperature profile ($y = 0.005$ m) is plotted at two different time instants, $t = 0.0005$ s and $t = 0.001$ s.

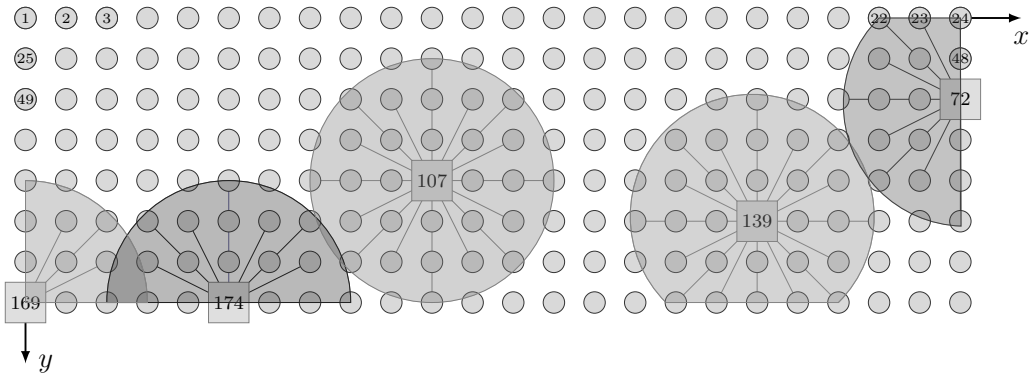

Figure 8: PD discretization of a 2D plate, using $\mathcal{N} = 192$ material points, $\Delta x = X/23$, $\Delta y = Y/7$ and $\delta = 3\Delta x$, hence $m = 3$. Thermal bonds for the 72^{nd},107^{th},139^{th}, $169^{\text{th}}$and 174^{th} material points are highlighted. The families of the highlighted points are evidenced, too.

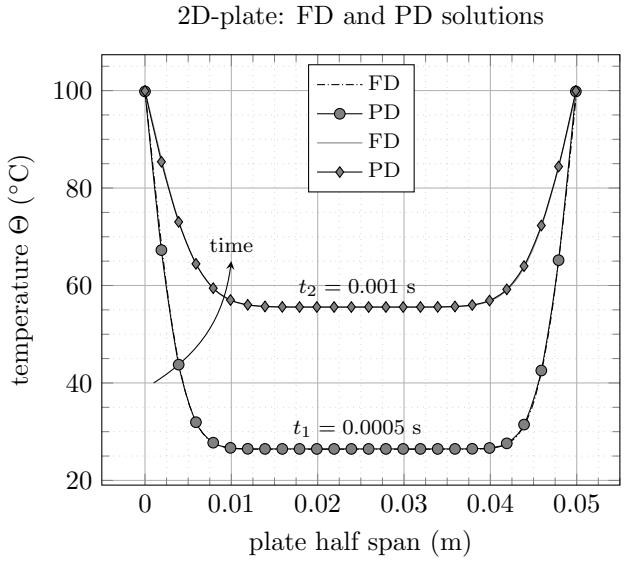

Figure 9: Comparison between the classical solution approximated with the finite differences method and the PD solution for two different time instants. The horizon size is $\delta = 3\Delta x$.

δ-convergence

A δ-convergence study has been performed in order to investigate the behaviour of the PD solution w.r.t. the classical one, thus Eq. 29 is used again. In Fig. 10 δ-convergence rates are shown for three different non-locality parameters ($m = 3\,, m = 4\,, m = 5$) and at two different time instants ($t = 0.0005$ s and $t = 0.001$ s). Since the PD solution has to converge to the classical one when $\delta \to 0$, the relative difference is expected to reduce when the horizon reduces. This behavior is confirmed by the results in Fig. 10. Furthermore, the relative difference is much smaller for $m = 3$ than for the other values, and this confirms that $m = 3$ is the optimal choice to approximate the local solution. However, the convergence rate is reduced to one, while in the 1D test case it was found to be equal to two, or even greater. Such a reduction can be attributed to the definition of the family of the point $\mathbf{x}_{(i)}$: while in a 1D problem with a regular discretization it is possible to perfectly include all the material points located at a distance smaller than δ, in a 2 or 3D problem there will certainly be some material points that are only partially included in the circle (or sphere) of radius δ. As suggested by Bobaru and Duangpanya (2012) this is likely the root cause of the reduction in the δ-convergence order from two to one. A solution to this problem has been proposed by Yu (2011, Sec. 2.4), who suggested to use an adaptive integration method method to compute the integral over the family of $\boldsymbol{x}_{(i)}$ and to take into account also the partially included particles (see also Madenci and Oterkus, 2014, Sec 7.2 for an alternative volume correction procedure).

3.3. Mesh sensitivity

The convergence studies performed so far were based on regular grids. It is nonetheless important to assess how the solution behaves with irregular grids, such as those that could be used to discretize irregular domains or that could arise when dealing with large displacements. The mesh sensitivity of the structural problem has already been studied by Henke and Shanbhag (2014). The same plate of Subsec. 3.2 is discretized as a 3D body and subjected to thermal shock boundary conditions on its lateral faces. The thermal shock is equal to $\Delta\Theta = -280$ °C. Both a regular and a randomly perturbed mesh are considered.

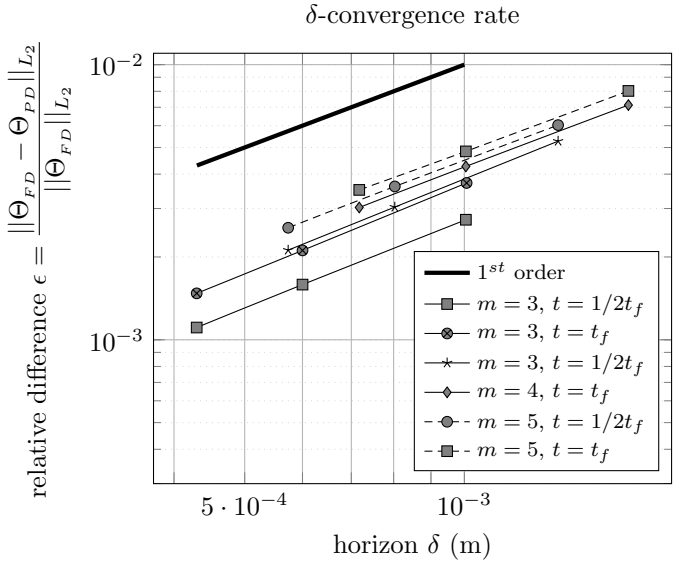

Figure 10: δ-convergence rate. First order of δ-convergence for all the values of m. A smaller relative difference is observed for smaller values of m, as expected.

Mesh Perturbation

The perturbed mesh is created starting from the definition of the element size

$$\texttt{elemSize} = \frac{\texttt{elemLength}_\texttt{x} + \texttt{elemLength}_\texttt{y} + \texttt{elemLength}_\texttt{z}}{3}. \tag{35}$$

The perturbation entity, `magnitude`, is defined as

$$\texttt{magnitude} = \epsilon \cdot \texttt{elemSize}, \tag{36}$$

with $0 < \epsilon < 0.5$. Choosing $\epsilon \geq 0.5$ would make possible the overlapping of two or more nodes, leading to the non-physical condition of material compenetration. Finally the x, y and z position components of every material particle are perturbed according to the following formula:

$$x_{(i)} = \big(2 \cdot \texttt{random}_\texttt{i}(0,1) - 1\big) \cdot \texttt{magnitude} \tag{37}$$

where $\texttt{random}_\texttt{i}(0,1)$ stands for a uniformly distributed random number between 0 and 1.

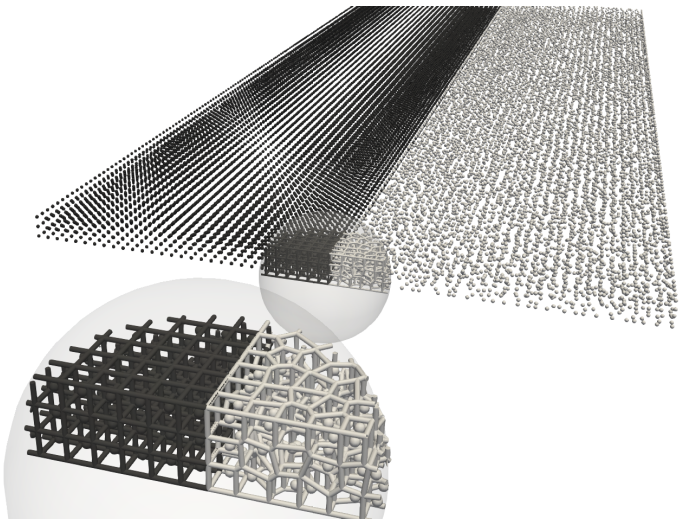

Figure 11: Non-perturbed (left half, black) and perturbed (right half, gray) discretized domain and detail of the corresponding Voronoi tessellation, $150 \times 30 \times 3$ points, `magnitude` $= 0.4 \cdot$ `elemSize`.

Voronoi tessellation

Since the distance between the particles is not constant for the irregular mesh, the volume associated to each material particle is defined as the volume of the convex polyhedron surrounding it. Thus, a Voronoi tessellation can be used to compute the volumes. Typical regular and irregular discretizations considered for this study are shown Fig. 11.

Mesh dependency study by varying the horizon

A plate with dimensions $X = 0.05$ m (length), $Y = 0.01$ m (height) and $Z = 0.001$ m (thickness) is discretized with 150 material points along the x axis, 30 points along the y axis and 3 points along the z axis. The following non-locality parameter values are chosen: $m = 3, 4, 5, 6, 7$; with a fixed discretization this corresponds to a change of horizon. The thermal diffusivity is $\gamma = 0.13$ W m^{-2} s^{-1}. The plate is subjected to thermal shock boundary conditions on its boundaries, with the initial temperature difference between the plate and the fluid at its lateral boundary equal $\Delta\Theta_{BC}(t = 0) = -280$ °C. Tab. 1 reports the temperature difference at time $\hat{t}_1 = 0.0001$ s and $\hat{t}_2 = 0.0002$ s between the non-perturbed and the perturbed mesh in the central point of the plate. The maximum temperature difference is equal to $\Delta\hat{\Theta}(t_f) = 6.1$ °C, corresponding to a relative error $\epsilon_{\%}(t_f) = 3.38\,\%$.

	$m=3$	$m=4$	$m=5$	$m=6$	$m=7$
$\Delta\hat{\Theta}(\frac{1}{2}t_f)$, °C	-4.3	4.8	3.5	-0.3	0.3
$\Delta\hat{\Theta}(t_f)$, °C	-6.1	3.4	1.8	3.0	3.1

Table 1: Temperature difference in the central point of the non-perturbed plate, i.e. in $\hat{x} = 0.025$ m, $\hat{y} = 0.005$ m, $\hat{z} = 0.0005$ m, at $\hat{t}_1 = \frac{1}{2}t_f$, $\hat{t}_2 = t_f$, where $t_f = 0.0002$ s. Temperature in such point is indicated with $\Theta(\hat{x}, \hat{y}, \hat{z}, \hat{t}) = \hat{\Theta}(\hat{t})$.

	$m=3$	$m=4$	$m=5$	$m=6$	$m=7$
$\epsilon_{\%}(t_f)$	3.38	2.45	1.23	2.02	2.14

Table 2: Percent error in $\hat{x} = 0.025$ m, $\hat{y} = 0.005$ m, $\hat{z} = 0.0005$ m, at $\hat{t} = t_f$, where $t_f = 0.0002$ s. Temperature in such point is indicated with $\Theta(\hat{x}, \hat{y}, \hat{z}, \hat{t}) = \hat{\Theta}(\hat{t})$.

The percent errors at $t = t_f = 0.0002$ s for different values of non-locality parameters are shown in Tab. 2. They are always moderate and below 3.5 %; this confirms that the peridynamic solution, for any horizon value, depends only marginally on the discretization adopted.

In Fig. 12 the solutions for both non-perturbed and perturbed meshes are plotted for the case $m = 3$ in the middle of the plate, i.e. for $y = 0.005$ m and $z = 0.0005$ m, as a function of x. The difference between the solutions at $x = 0.025$ m is equal to the 6.1 °C reported in Tab. 1, with the relative error $\epsilon_{\%} = 3.38\%$ of Tab. 2.

4. Thermo-mechanic test cases

Two thermo-mechanical problems with thermal shock boundary conditions are investigated. The first case study (Example 1) involves an alumina slab subjected to thermal shock on its lateral faces. The second case study (Example 2) deals with a thick plate subjected to a thermal shock on its lower face.

4.1. Example 1

A plate with the properties of Tab. 3 is subjected to a thermal shock on its lateral faces. The initial temperature difference between the fluid and the wall is $\Delta\Theta = -280\,°\text{C}$ in the first case, $\Delta\Theta = -380\,°\text{C}$ in the second case and $\Delta\Theta = -580°\text{C}$ in the third case. The experiments of Shao et al. (2011) have shown that a regular pattern of cracks orthogonal to the boundaries arises, see also the results obtained by Li et al. (2013). The number

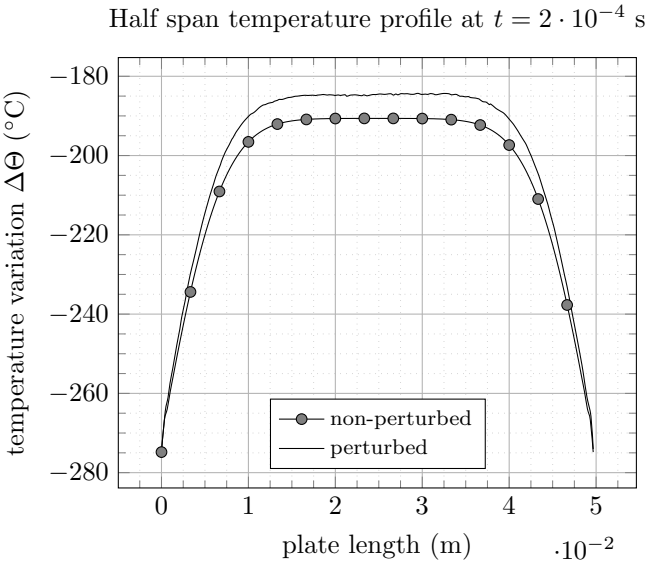

Figure 12: Temperature profile along the plate half span due to thermal shock, considering $m = 3$ and dividing the domain in 150 material points along the x axis, i.e. $\delta \simeq 0.002$ m.

specific heat	880 J kg^{-1} K^{-1}
thermal expansion coeff.	7.2 μK^{-1}
thermal conductivity	18 W m^{-1} K^{-1}
bulk modulus	227 GPa
shear modulus	136 GPa
density	3950 kg m^{-3}
fracture toughness	42.27 J m^{-2}
width X	50 mm
depth Y	10 mm
thickness Z	1 mm

Table 3: Mechanical, thermal and geometric properties of the domain under exam.

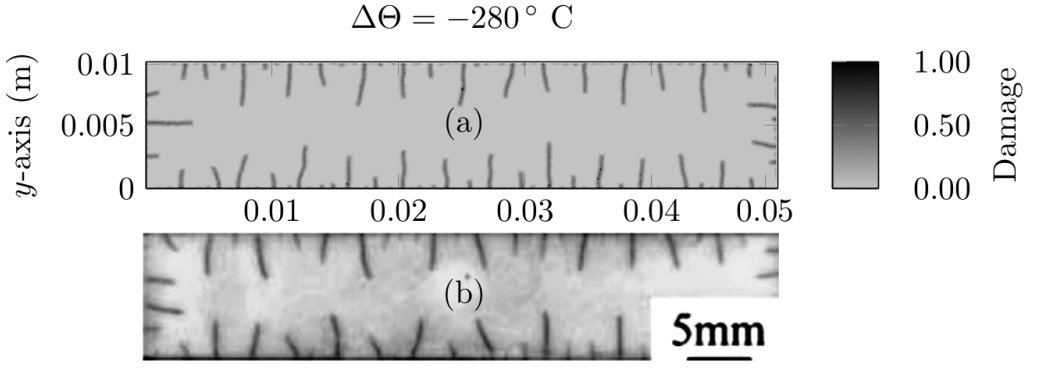

Figure 13: Thermal shock with an initial temperature difference $\Delta\Theta = -280\,^\circ$C; top: peridynamic simulation; bottom: experimental results by Shao et al. (2011).

of cracks and the medium crack depth increases as the initial temperature difference is increased; however, the cracks do not coalesce. Experimental results from Shao et al. (2011) are shown in Fig. 13(b) ($\Delta\Theta = -280\,^\circ$C), Fig. 15(b) ($\Delta\Theta = -380\,^\circ$C) and Fig. 17(b) ($\Delta\Theta = -580\,^\circ$C). The peridynamic discretization is the same for the first two cases, with the plate subdivided in 171 500 material points, specifically 350 through its width, 70 through its depth and 7 through its thickness, as shown in Fig. 11. The integration time step is equal to $\Delta t^{ME} = 10.433$ ns, with a mechanical problem critical time step $\Delta t^{ME}_{cr} = 13.041$ ns and a thermal problem critical time step $\Delta t^{TH}_{cr} = 2.827$ ms. The third case, characterized by higher temperature gradient, required a finer $700 \times 140 \times 14$ mesh, with 1372000 points and halved time steps, to get correct results.

As regards the $\Delta\Theta = -280\,^\circ$C case, numerical and experimental results are in qualitative agreement: as shown in Fig. 13 both the experiment and the simulation are characterized by a pattern of almost equally spaced cracks orthogonal to the free surfaces, with shorter cracks interposed between the longer ones. Note that the PD model does not require any a priori hypothesis neither about the cracks nucleation points nor about their direction of propagation. A quantitative analysis of the crack frequency, considering only cracks whose depth w is greater than 10% of the plate half width, i.e. $w > 0.1 \cdot Y/2$, is shown in the bar diagram of Fig. 14. We observed that the results showed by Shao et al. (2011) overestimated the number of cracks per non-dimensionalized length both with respect to what has emerged in this work and with respect to the frequencies that can be computed by an-

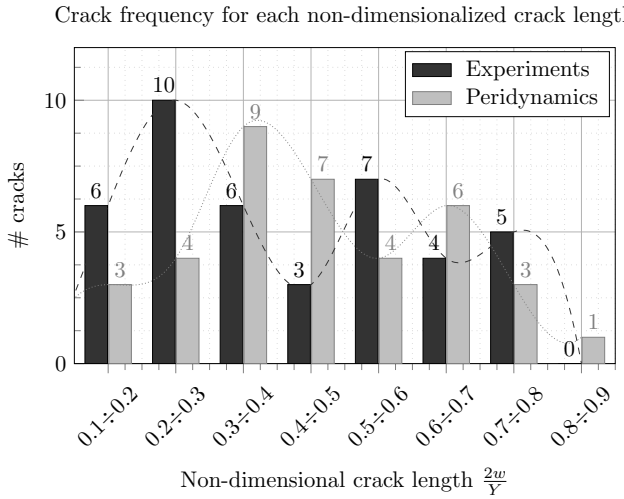

Figure 14: Crack frequency diagram and spline interpolation of results for $\Delta\Theta = -280\,^{\circ}\mathrm{C}$.

alyzing the image of that same paper. For this reason we recomputed the crack lengths by post-processing the images of Shao et al. (2011). As shown in Fig. 14, the peridynamic solution does differ from the experiments: even if the overall number of crack is the same, the experiment has a maximum number of cracks for a non-dimensional crack length $2w/Y = 0.2 \div 0.3$, while the peridynamic model has a less pronounced maximum for $2w/Y = 0.3 \div 0.4$. Figures 15 and 16 show the corresponding results obtained for $\Delta\Theta = -380\,^{\circ}\mathrm{C}$. In this case the results of Fig. 16 show a better frequency match between the experiment and the simulation. Even better results are obtained for $\Delta\Theta = -580\,^{\circ}\mathrm{C}$, see Figs. 17 and 18, although this is likely helped by the finer discretization. After comparing the three cases one could be tempted to infer that the peridynamic model is better suited to reproduce the effects of strong thermal shocks, while it is not able to correctly account for shorter, slowly propagating cracks, at least with the adopted discretization. Another explanation, however, could be that the experimental statistical base is not sufficient, and that the experimental results dispersion could be higher for lower temperature differences; as a matter of fact, no statistical data are available from Shao et al. (2011). Note that, although the crack frequency diagrams correlation may not seem very good at lower temperatures, it compares favorably with similar diagrams obtained by Li et al. (2013). Note also that the overall number of cracks is correctly predicted for all the three cases. A perhaps better assessment of the simulation accuracy can be achieved by

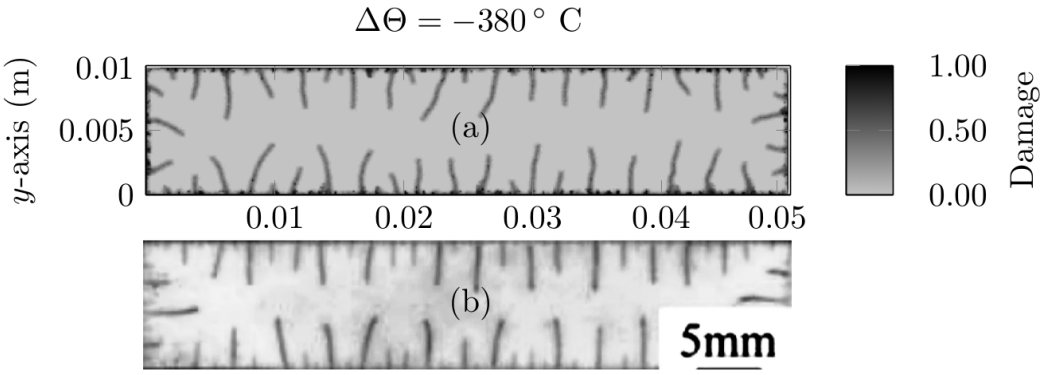

Figure 15: Thermal shock with an initial temperature difference of $\Delta\Theta = -380\,^\circ$C; top: peridynamic simulation; bottom: experimental results by Shao et al. (2011).

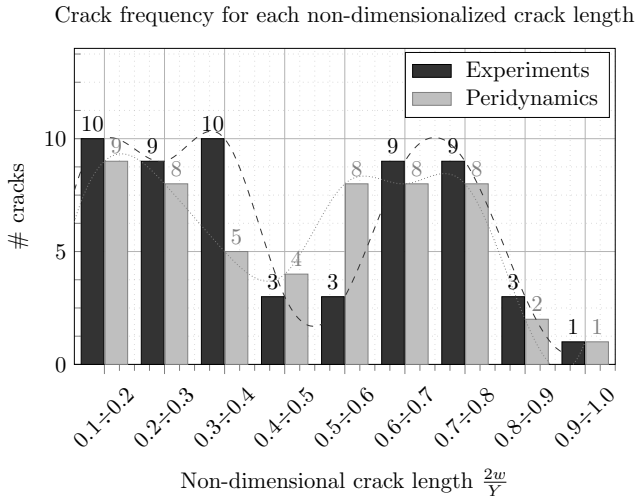

Figure 16: Crack frequency diagram and spline interpolation of results for $\Delta\Theta = -380\,^\circ$C.

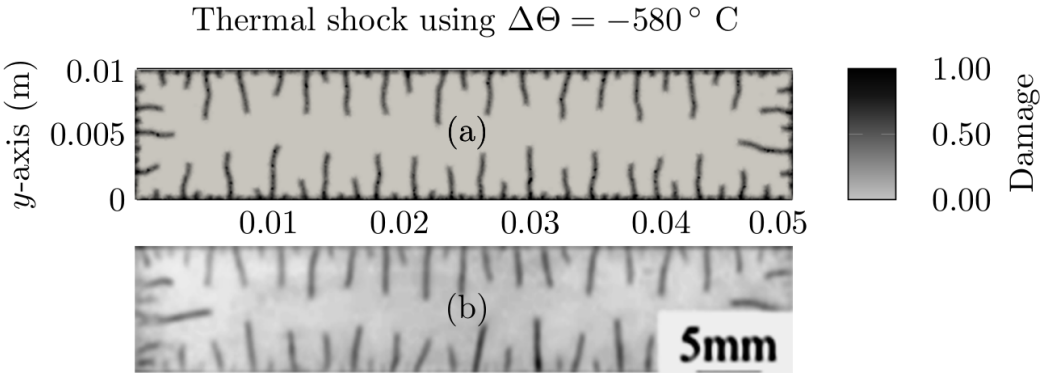

Figure 17: Thermal shock with an initial temperature difference of $\Delta\Theta = -580\,^\circ$C; top: peridynamic simulation; bottom: experimental results by Shao et al. (2011).

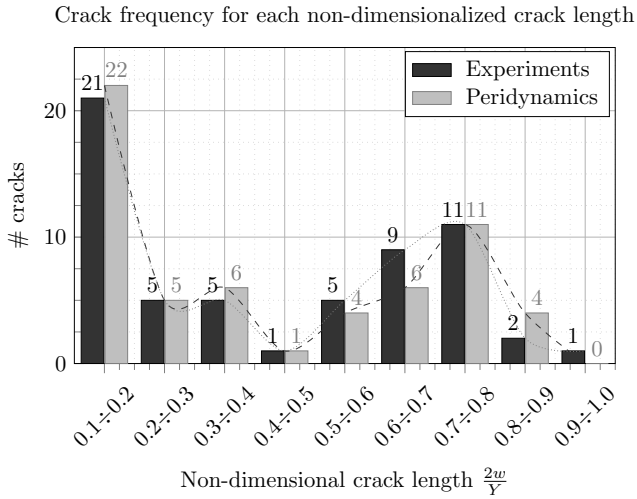

Figure 18: Crack frequency diagram and spline interpolation of results for $\Delta\Theta = -580\,^\circ$C.

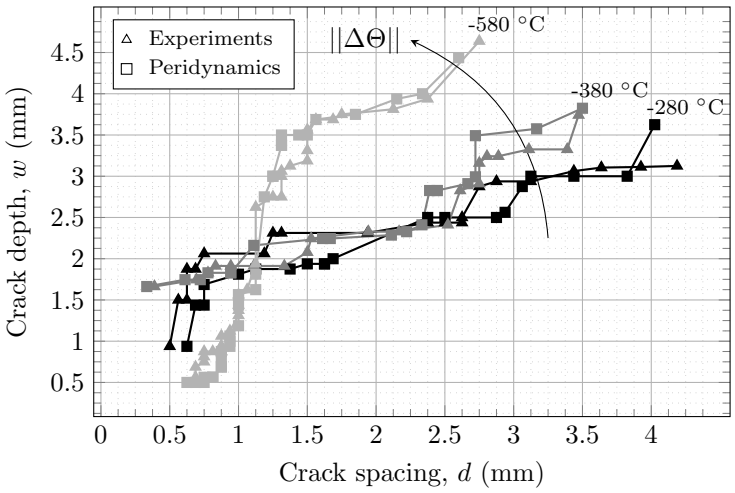

Figure 19: Crack depth as a function of crack spacing.

following Bourdin et al. (2013), who compare their simulations with the experimental results of Shao et al. (2011) by plotting the crack depth as a function of the crack spacing. The same comparison is reported in Fig. 19, where the "Experiments" data are obtained by us by analyzing Shao et al.'s figures. The overall trend is well matched, both qualitatively and quantitatively, for all the three shock temperatures. Essentially the same results, not shown here for conciseness, are obtained with irregular grids, built by following the procedure of Subsec. 3.3.

With uncoupled simulations, such as those performed by Bourdin et al. (2013), the temperature profile can be computed, as a known function of time, independently from the structural response. Here, instead, the heat flux inside the material is blocked by cracks, see Eq. 15, and the reached temperature distribution does depend also on the damage state of the slab. Hence, the temperature is characterized by discontinuities along fully developed cracks, as in Fig. 20. This effect appears to be more significant for the third thermal shock case with $\Delta\Theta = -250\,^{\circ}\mathrm{C}$. This case, not simulated by other authors, is characterized by a pronounced bends of the cracks. Figure 21 compares the cracks predicted by the peridynamic code when the heat is free to flow trough the cracks (top, uncoupled peridynamic simulation) and when it is blocked by cracks (middle, weakly coupled peridynamic simulation. It is clear the the uncoupled simulation results are qualitatively different from the coupled ones, that better matches the bent cracks of the

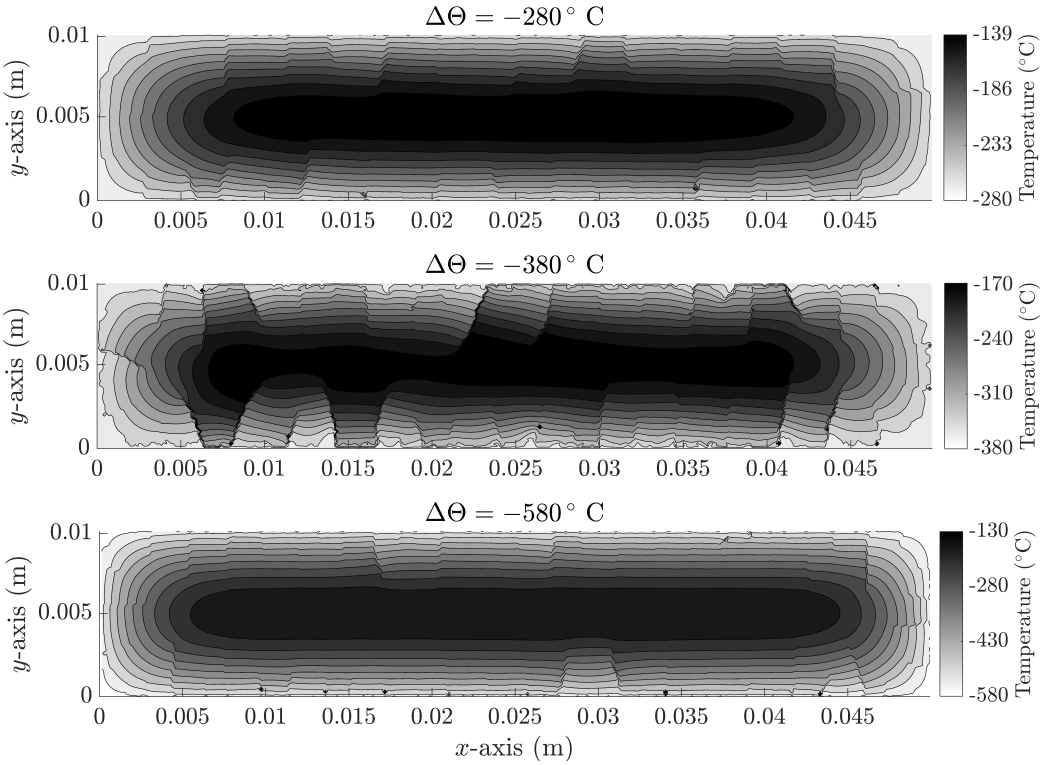

Figure 20: Temperature profiles due to a peridynamic thermo-mechanical simulation, results after $t \simeq 5$ s. Note the discontinuities in correspondence of the cracks.

experiment (bottom, experimental results). The corresponding temperature fields are compared in Fig. 22, with the coupled simulation showing significant temperature jumps across all the bent cracks.

4.2. Example 2

A thick slab made of fragile material with the geometric, thermal and mechanical properties of Tab. 4 is subjected to a thermal shock on its lower face. The initial temperature difference between the fluid and the slab is $\Delta\Theta = -500\,^{\circ}$C. The integration time step is equal to $\Delta t^{ME} = 10$ ns, with a mechanical problem critical time step $\Delta t^{ME}_{cr} = 18.938$ ns and a thermal problem critical time step $\Delta t^{TH}_{cr} = 5.962$ ms. This thermo-mechanical problem shows a peculiar crack evolution known as columnar jointing. Columnar jointing is a geologic structure where sets of closely spaced fractures, referred to as joints, form a regular array of polygonal prisms, addressed as columns.

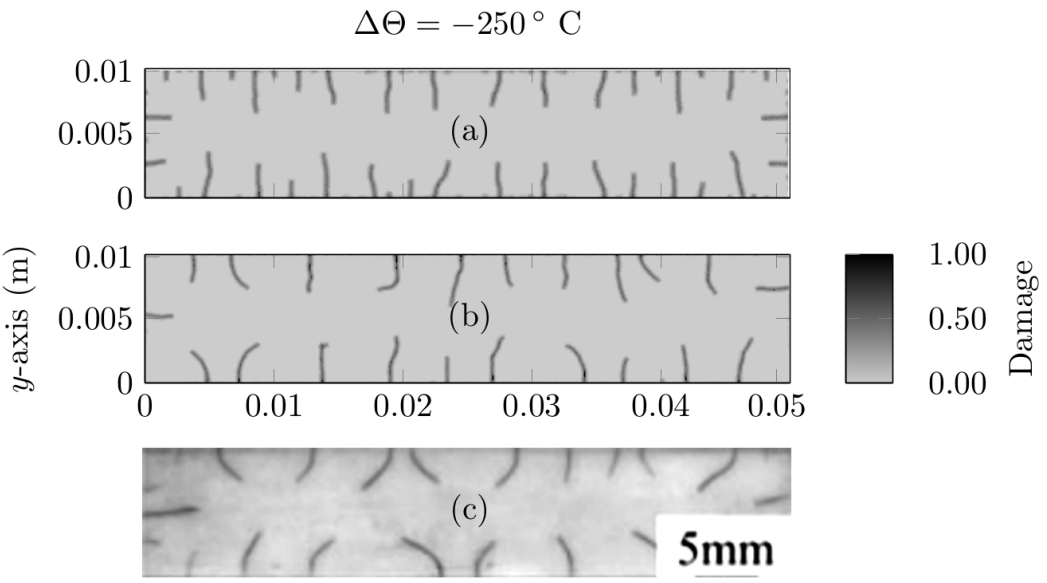

Figure 21: Thermal shock with an initial temperature difference of $\Delta\Theta = -250\,^\circ$C. top: uncoupled peridynamic simulation; middle: weakly coupled peridynamic simulation; bottom experimental results by Shao et al. (2011).

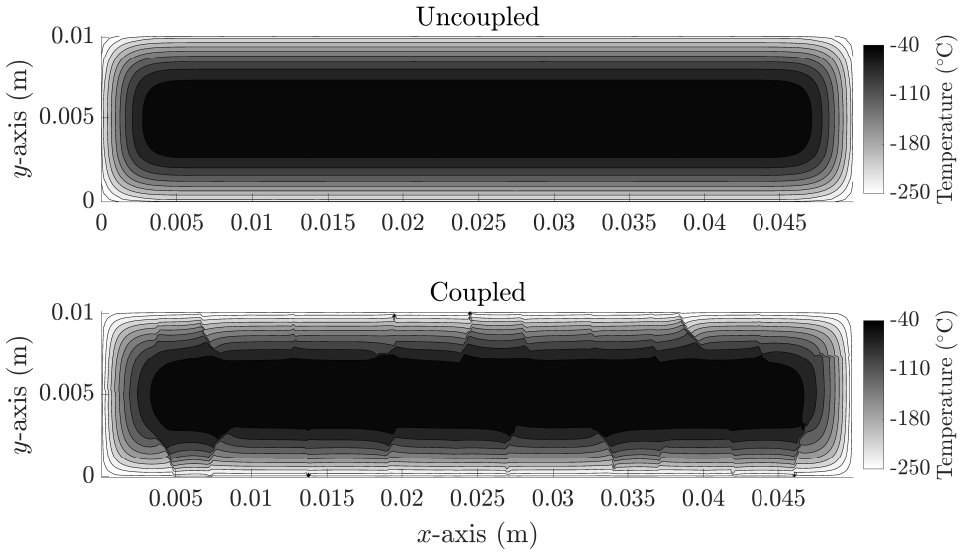

Figure 22: Temperature profile due to a peridynamic thermo-mechanical simulation; top: uncoupled simulation; bottom: weakly-coupled simulation.

specific heat	880 J kg^{-1} K^{-1}
thermal expansion coeff.	7.2 μK^{-1}
thermal conductivity	18 W m^{-1} K^{-1}
bulk modulus	227 GPa
shear modulus	136 GPa
density	3950 kg m^{-3}
fracture toughness	42.27 J m^{-2}
width X	6 cm
depth Y	6 cm
thickness Z	2 cm

Table 4: Mechanical, thermal and geometric properties of the domain under exam.

Many studies about this fascinating phenomenon can be found in literature; the reader can find further details about columnar jointing in e.g. Beard (1959); Spry (1962); Jagla and Rojo (2002); Bahr et al. (2009); Goehring et al. (2009); Bourdin et al. (2013). The onset and propagation of basalt columnar cracks is often modeled by resorting to fracture mechanics or to the finite elements method. Energy minimization can be invoked to justify the polygonal structure of columnar basalts. Jagla and Rojo (2002) showed that if one considers a small increase in the crack length, the perfect hexagonal pattern relieves the maximum amount of elastic energy for a given total length of fractures. Later on, Jungen (2012) proposed a variational approach in which the fundamental hypothesis is that a fracture nucleates to minimize the total amount of stored elastic energy in the system. Columnar jointing has already been simulated numerically with good results. For example, Bourdin et al. (2013) proposed a quasi-static gradient damage model that leads to the well-known complex crack pattern, with many small cracks joining together and arranging themselves into a prismatic patter after reaching a certain depth through the domain thickness. Bourdin et al.'s typical result, obtained with 44e+6 degrees of freedom and using 1536 cores of the NSF-XSEDE cluster Stampede at Texas Advanced Computing Center, is shown in Fig. 23. The present peridynamic model makes use of 4.5e6 material points arranged in a regular pattern; the horizon is chosen to be $\delta = 3X/299 \simeq 0.6$ mm, therefore $m = \delta/\Delta x = 3$. The computation was performed on four cores of a standard desktop pc, using an Intel® Core(TM) i7 950 (3.07 GHz); the explicit integration took almost 18 h. The resulting crack pattern is shown in Fig. 24. A

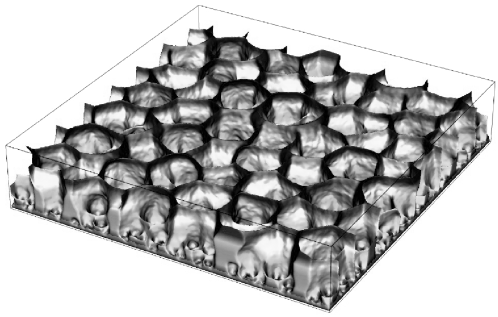

Figure 23: Columnar jointing computed using a quasi-static gradient damage model; image taken from Bourdin et al. (2013).

dense pattern of small cracks nucleates on the lower face of the slab. After that, the cracks propagate through the domain thickness; after reaching a depth of $z \approx 3$ mm the propagation becomes stable, with the typical hexagonal pattern and the formation of columns. Finally, the somewhat reduced thickness of the specimen, limited by the computational resources at hand, leads to the propagation of two major transverse crack that almost break it in four parts. The simulated crack pattern is compared, in Fig. 25, with a typical basalt formation. By taking slices of the mesh at different heights it is possible to identify the joining of smaller columns into bigger ones, a phenomenon described e.g. by Bahr et al. (2009), see Fig. 26. The sequence of Fig. 27 shows the joining of three columns. This joining can occur multiple times throughout the thickness of the slab, as shown in Fig. 28.
Figure 29 shows the crack pattern obtained for an stronger thermal shock of $\Delta\Theta = -800\,^{\circ}\mathrm{C}$. Following again Bourdin et al. (2013), Fig. 30 plots the average crack size $d = \sqrt{A}$, where A is the average column area at a given height, as a function of the distance a from the exposed face. Data are in good agreement with the two-dimensional scaling law of Bahr et al. (2010), both for the $\Delta\Theta = -500\,^{\circ}\mathrm{C}$. and the $\Delta\Theta = -800\,^{\circ}\mathrm{C}$ cases. The same Figure reports for completeness all the numerical results obtained by Bourdin et al. (2013) for a wider set of lengths of the slab side.

5. Concluding remarks

The proposed weakly coupled peridynamic formulation allows to effectively simulate the onset of 2D and 3D mode-I thermally-induced cracks. No prior knowledge of the cracks number, point of initiation, direction of prop-

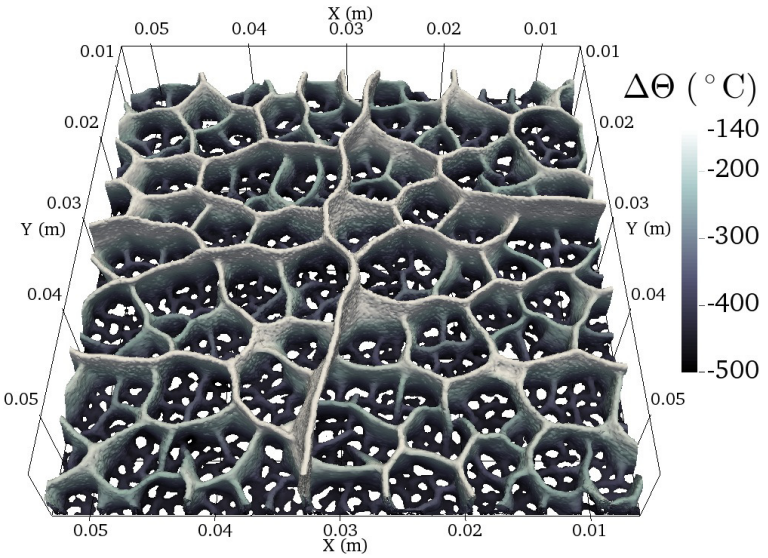

Figure 24: Peridynamic simulation of columnar jointing, considering a thick slab, $\Delta\Theta = -500\,^{\circ}\mathrm{C}$.

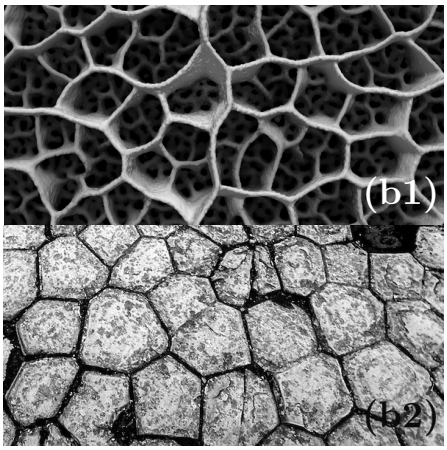

Figure 25: Peridynamic simulation (b1) and real basalt (b2) cracks.

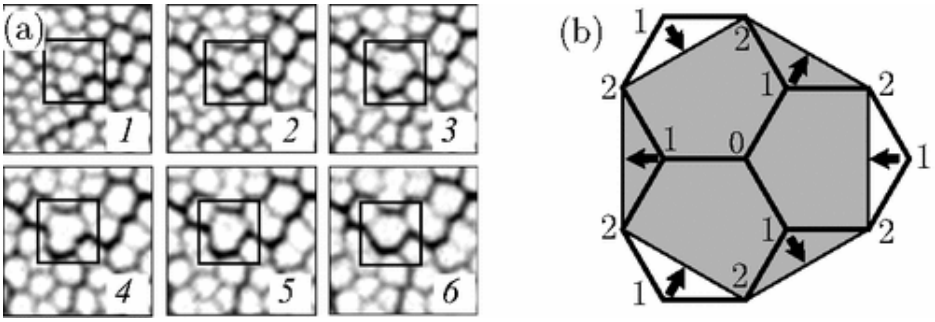

Figure 26: Sequence of slices through a tomogram of columnar joints growing into the depth of drying corn starch slurry (22a) and idealized interpretation of the joining mechanism (22b). Images taken from Bahr et al. (2009).

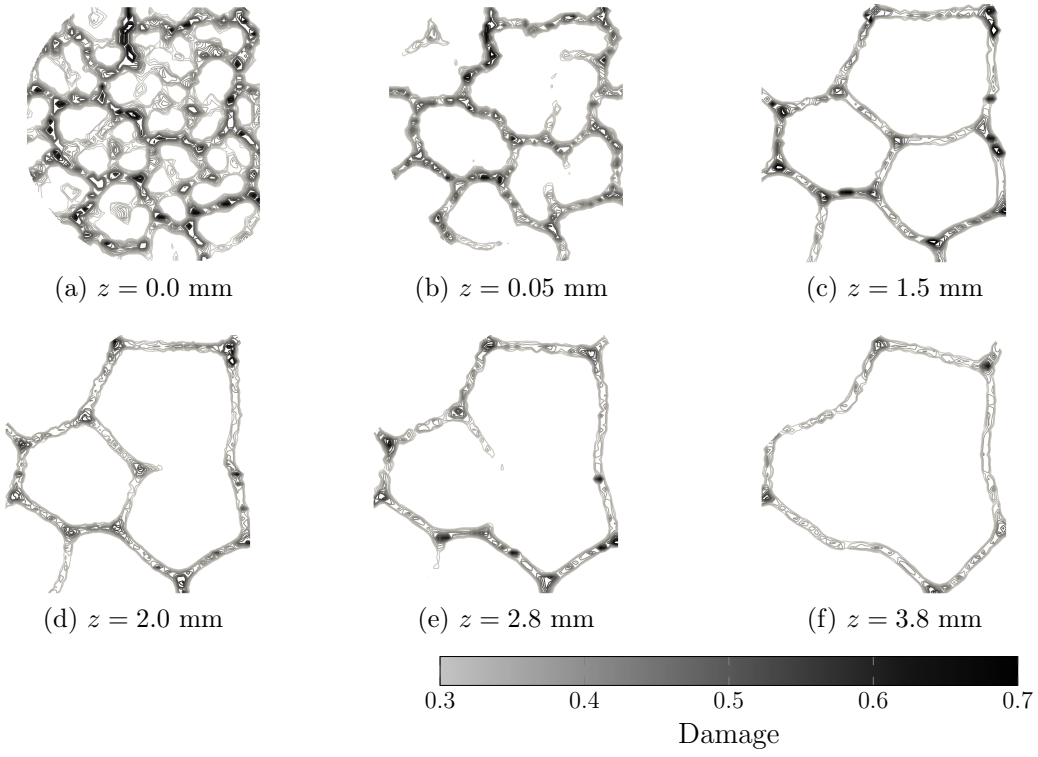

Figure 27: Three columns merge into one through the thickness of the slab.

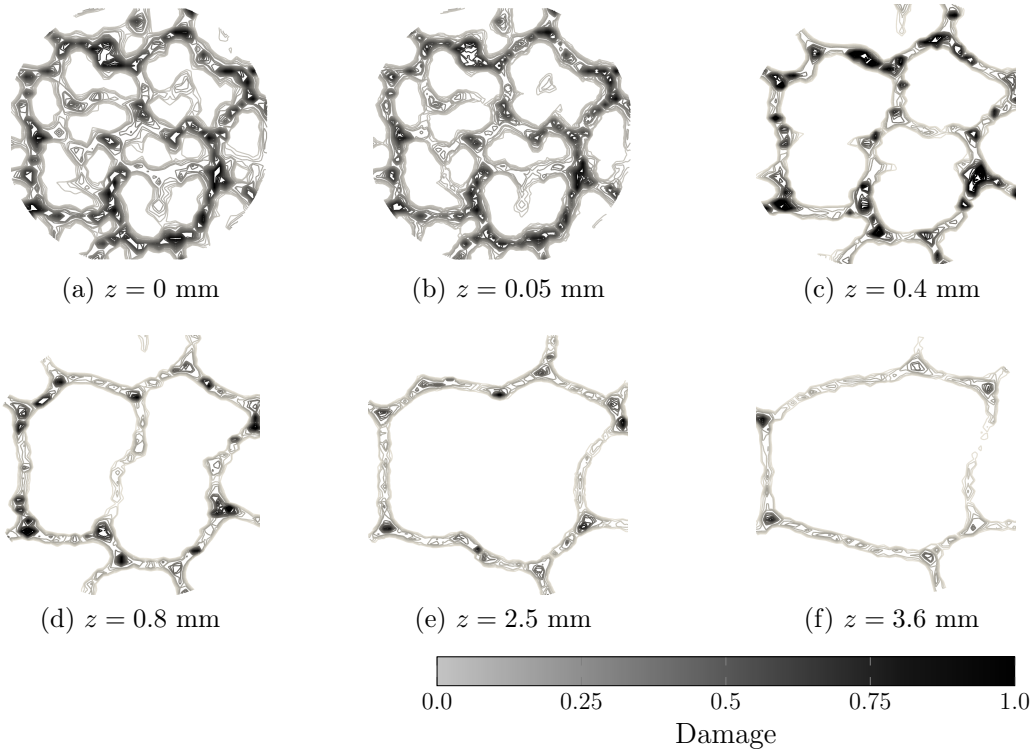

(a) $z = 0$ mm (b) $z = 0.05$ mm (c) $z = 0.4$ mm

(d) $z = 0.8$ mm (e) $z = 2.5$ mm (f) $z = 3.6$ mm

Figure 28: Merging of three columns occurring twice through the slab thickness: first merge from (28a) to (28c), second merge from (28c) to (28f).

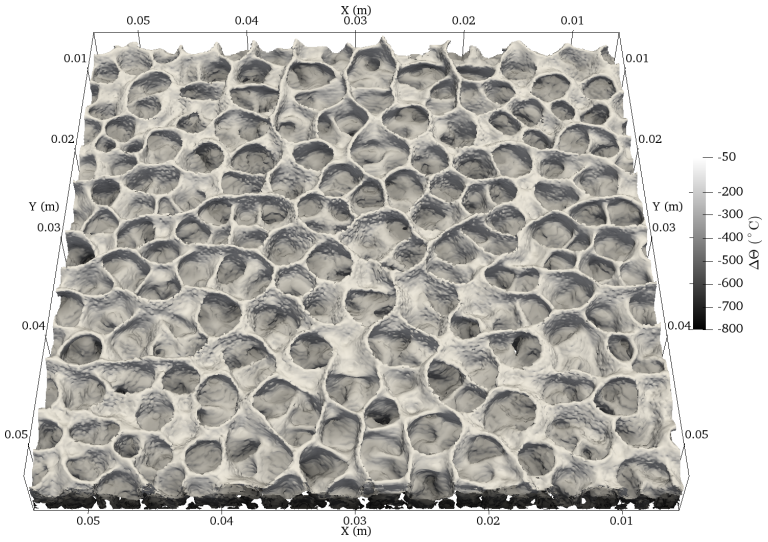

Figure 29: Peridynamic simulation of columnar jointing, considering a thick slab, $\Delta\Theta = -800\,^{\circ}\mathrm{C}$.

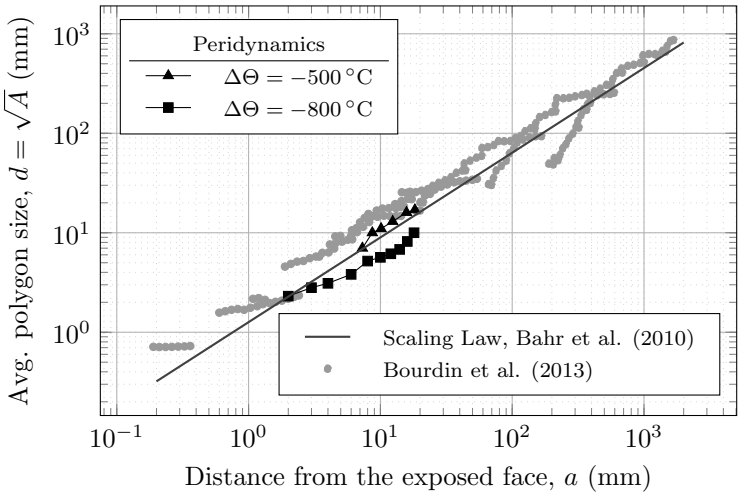

Figure 30: Average crack size as a function of distance from the exposed face.

agation or size is needed. Due to the remarkably different time scales of the mechanics and thermal subsystems the explicit integration scheme requires a multirate approach. That said, the overall computation effort and the results obtained are comparable with those of the competing implicit approach proposed by Bourdin et al. (2013).

A peculiarity of the implementation is that the predicted temperature distribution does depend on the cracks onset; it is thus different from what one would obtain by independently integrating the mechanical and thermal subsystems, as Figs. 20 and 22 make clear. The assumption of Eq. 15, where the heat flux is prevented by the mechanical damage, may be deemed reasonable for opening mode-I crack; it should however be critically evaluated, and possibly modified with the introduction of appropriated contact conductance terms, whenever closing and/or mode-II and mode-III cracks have to be accounted for.

References

Agwai, A. G., 2011. A peridynamic approach for coupled fields. Ph.D. thesis, The University of Arizona.

Amani, J., Oterkus, E., Areias, P., Zi, G., Nguyen-Thoi, T., Rabczuk, T., 2016. A non-ordinary state-based peridynamics formulation for thermoplastic fracture. International Journal of Impact Engineering 87, 83–94.

Bahr, H.-A., Hofmann, M., Weiss, H.-J., Bahr, U., Fischer, G., Balke, H., 2009. Diameter of basalt columns derived from fracture mechanics bifurcation analysis. Physical Review E 79 (5), 056103.

Bahr, H.-A., Weiss, H.-J., Bahr, U., Hofmann, M., Fischer, G., Lampenscherf, S., Balke, H., 2010. Scaling behavior of thermal shock crack patterns and tunneling cracks driven by cooling or drying. Journal of the Mechanics and Physics of Solids 58 (9), 1411–1421.

Beard, C. N., 1959. Quantitative study of columnar jointing. Geological Society of America Bulletin 70 (3), 379–382.

Belytschko, T., Krongauz, Y., Organ, D., Fleming, M., Krysl, P., Dec. 1996. Meshless methods: An overview and recent developments. Computer Methods in Applied Mechanics and Engineering 139 (1), 3–47.

Bobaru, F., Duangpanya, M., 2010. The peridynamic formulation for transient heat conduction. International Journal of Heat and Mass Transfer 53 (19), 4047–4059.

Bobaru, F., Duangpanya, M., 2012. A peridynamic formulation for transient heat conduction in bodies with evolving discontinuities. Journal of Computational Physics 231 (7), 2764–2785.

Bobaru, F., Yang, M., Alves, L. F., Silling, S. A., Askari, E., Xu, J., 2009. Convergence, adaptive refinement, and scaling in 1d peridynamics. International Journal for Numerical Methods in Engineering 77 (6), 852–877.

Bourdin, B., Marigo, J.-j., Maurini, C., Sicsic, P., 2013. Morphogenesis and propagation of complex cracks induced by thermal shocks. Physical review letters 112 (1), 014301.

Curtin, W. A., Scher, H., Mar. 1990. Brittle fracture in disordered materials: A spring network model. Journal of Materials Research 5 (3), 535–553. URL https://www.cambridge.org/core/journals/journal-of-materials-research/artic

de Borst, R., Gutiérrez, M. A., Wells, G. N., Remmers, J. J., Askes, H., 2004. Cohesive-zone models, higher-order continuum theories and reliability methods for computational failure analysis. International Journal for Numerical Methods in Engineering 60 (1), 289–315.

Demmie, P., Silling, S., 2007. An approach to modeling extreme loading of structures using peridynamics. Journal of Mechanics of Materials and Structures 2 (10), 1921–1945.

Gear, C. W., Wells, D., 1984. Multirate linear multistep methods. BIT Numerical Mathematics 24 (4), 484–502.

Gerstle, W., Sau, N., Silling, S., 2007. Peridynamic modeling of concrete structures. Nuclear engineering and design 237 (12), 1250–1258.

Goehring, L., Mahadevan, L., Morris, S. W., 2009. Nonequilibrium scale selection mechanism for columnar jointing. Proceedings of the National Academy of Sciences 106, 387–392.

Hayakawa, Y., Mar. 1994a. Numerical study of oscillatory crack propagation through a two-dimensional crystal. Physical Review E 49 (3), R1804–R1807.
URL https://link.aps.org/doi/10.1103/PhysRevE.49.R1804

Hayakawa, Y., Sep. 1994b. Pattern selection of multicrack propagation in quenched crystals. Physical Review E 50 (3), R1748–R1751.
URL https://link.aps.org/doi/10.1103/PhysRevE.50.R1748

Henke, S. F., Shanbhag, S., 2014. Mesh sensitivity in peridynamic simulations. Computer Physics Communications 185 (1), 181–193.

Jagla, E., Rojo, A., 2002. Sequential fragmentation: The origin of columnar quasihexagonal patterns. Physical Review E 65 (2), 026203.

Jungen, M., 2012. A model of columnar jointing. Mathematical Models and Methods in Applied Sciences 22 (02), 1150006.

Kalthoff, J., Winkler, S., 1988. Failure mode transition at high rates of shear loading. DGM Informationsgesellschaft mbH, Impact Loading and Dynamic Behavior of Materials 1, 185–195.

Kilic, B., Madenci, E., 2009. Prediction of crack paths in a quenched glass plate by using peridynamic theory. International journal of fracture 156 (2), 165–177.

Li, J., Song, F., Jiang, C., nov 2013. Direct numerical simulations on crack formation in ceramic materials under thermal shock by using a non-local fracture model. Journal of the European Ceramic Society 33 (13–14), 2677–2687.

Madenci, E., Oterkus, E., 2014. Peridynamic theory and its applications. Springer.

Madenci, E., Oterkus, S., 2016. Ordinary state-based peridynamics for plastic deformation according to von mises yield criteria with isotropic hardening. Journal of the Mechanics and Physics of Solids 86, 192–219.

Moës, N., Belytschko, T., 2002. Extended finite element method for cohesive crack growth. Engineering fracture mechanics 69 (7), 813–833.

Nguyen, V. P., Rabczuk, T., Bordas, S., Duflot, M., Dec. 2008. Meshless methods: A review and computer implementation aspects. Mathematics and Computers in Simulation 79 (3), 763–813.

Nishimoto, A., Mizuguchi, T., Kitsunezaki, S., Jul. 2007. Numerical study of drying process and columnar fracture process in granule-water mixtures. Physical Review E 76 (1), 016102.
URL https://link.aps.org/doi/10.1103/PhysRevE.76.016102

O'Grady, J., Foster, J., 2014. Peridynamic plates and flat shells: A non-ordinary, state-based model. International Journal of Solids and Structures 51 (25-26), 4572–4579.

Oterkus, S., Madenci, E., May 2017. Peridynamic modeling of fuel pellet cracking. Engineering Fracture Mechanics 176, 23–37.
URL http://www.sciencedirect.com/science/article/pii/S0013794416305471

Park, M. L., Littlewood, D. J., Silling, S. A., 2012. Peridigm Users' Guide. Technical report SAND2012-7800, Sandia National Laboratories.

Rabczuk, T., Belytschko, T., Dec. 2004. Cracking particles: a simplified meshfree method for arbitrary evolving cracks. International Journal for Numerical Methods in Engineering 61 (13), 2316–2343.
URL http://onlinelibrary.wiley.com/doi/10.1002/nme.1151/abstract

Ren, H., Zhuang, X., Cai, Y., Rabczuk, T., Dec. 2016. Dual-horizon peridynamics. International Journal for Numerical Methods in Engineering 108 (12), 1451–1476.
URL http://onlinelibrary.wiley.com/doi/10.1002/nme.5257/abstract

Savcenco, V., Mattheij, R., 2010. Multirate numerical integration for stiff odes. In: Progress in Industrial Mathematics at ECMI 2008. Springer, pp. 327–332.

Seleson, P., Parks, M., 2011. On the role of the influence function in the peridynamic theory. International Journal of Multiscale Computational Engineering 9 (6), 689–706.

Seny, B., Lambrechts, J., Toulorge, T., Legat, V., Remacle, J.-F., 2014. An efficient parallel implementation of explicit multirate runge–kutta schemes

for discontinuous galerkin computations. Journal of Computational Physics 256, 135–160.

Shao, Y., Zhang, Y., Xu, X., Zhou, Z., Li, W., Liu, B., 2011. Effect of crack pattern on the residual strength of ceramics after quenching. Journal of the American Ceramic Society 94, 2804–2807.

Silling, S., 2003. Dynamic fracture modeling with a meshfree peridynamic code. Computational fluid and solid mechanics 2003, 641–644.

Silling, S., Lehoucq, R., 2010. Peridynamic theory of solid mechanics. Advances in Applied Mechanics 44, 73–168.

Silling, S. A., 2000. Reformulation of elasticity theory for discontinuities and long-range forces. Journal of the Mechanics & Physics of Solids 48 (1), 175–209.

Silling, S. A., Mar. 2010. Linearized Theory of Peridynamic States. Journal of Elasticity 99 (1), 85–111.
URL https://link.springer.com/article/10.1007/s10659-009-9234-0

Silling, S. A., Askari, E., 2004. Peridynamic modeling of impact damage. In: ASME/JSME 2004 Pressure Vessels and Piping Conference. American Society of Mechanical Engineers, pp. 197–205.

Silling, S. A., Askari, E., 2005. A meshfree method based on the peridynamic model of solid mechanics. Computers & structures 83 (17), 1526–1535.

Silling, S. A., Epton, M., Weckner, O., Xu, J., Askari, E., 2007. Peridynamic states and constitutive modeling. Journal of Elasticity 88 (2), 151–184.

Spry, A., 1962. The origin of columnar jointing, particularly in basalt flows. Journal of the Geological Society of Australia 8 (2), 191–216.

Tupek, M., Radovitzky, R., Apr. 2014. An extended constitutive correspondence formulation of peridynamics based on nonlinear bond-strain measures. Journal of the Mechanics and Physics of Solids 65, 82–92.
URL http://www.sciencedirect.com/science/article/pii/S0022509614000027

Warren, T. L., Silling, S. A., Askari, A., Weckner, O., Epton, M. A., Xu, J., 2009. A non-ordinary state-based peridynamic method to model solid material deformation and fracture. International Journal of Solids and Structures 46 (5), 1186–1195.

Wells, G., Sluys, L., 2001. A new method for modelling cohesive cracks using finite elements. International Journal for Numerical Methods in Engineering 50 (12), 2667–2682.

Wittel, F. K., Kun, F., KrÃ¶plin, B.-H., Herrmann, H. J., Nov. 2003. A study of transverse ply cracking using a discrete element method. Twelfth International Workshop on Computational Mechanics of Materials 28 (3), 608–619.
URL http://www.sciencedirect.com/science/article/pii/S0927025603001459

Yu, K., 2011. Enhanced integration methods for the peridynamic theory. Kansas State University.